Observed Characteristics of the Tornadic Supercells of 27–28 April 2011 in the Southeast United States

ANTHONY W. LYZA,[a,b] MATTHEW D. FLOURNOY,[a,b] AND ERIK N. RASMUSSEN[b]

[a] *Cooperative Institute for Severe and High-Impact Weather Research and Operations, University of Oklahoma, Norman, Oklahoma*
[b] *NOAA/OAR National Severe Storms Laboratory, Norman, Oklahoma*

ABSTRACT: An historic outbreak of tornadoes impacted a large swath of the eastern United States on 26–28 April 2011. The most severe series of tornadoes was associated with numerous classic supercell thunderstorms that developed across the Southeast during the afternoon and evening of 27 April and continued into the predawn of 28 April. This study documents characteristics of these storms with respect to tornado production and mesocyclone strength during different periods of each storm's life cycle. The supercells initiated in four quasi-distinct spatiotemporal regions, with each cluster exhibiting slightly different evolutionary traits and tornado production. These included differences in the mean times between convection initiation and the time of first tornadogenesis for each supercell, as well as variations in overall and significant tornado production. This suggests that mesoscale environmental differences, such as proximity to a mesoscale boundary, and/or storm-scale events strongly influenced the variety of supercell evolutionary paths that were observed during this event, even in the presence of a synoptic-scale background environment extremely favorable for supercell and tornado production. The azimuthal shear products from the Multi-Year Reanalysis of Remotely Sensed Storms database perform well in discriminating between mesocyclones associated with ongoing weak, strong, and violent tornadoes during the event. Furthermore, mean azimuthal shear values during pre-tornadic (e.g., within 30 min of tornadogenesis) and tornadic phases are significantly larger than those during nontornadic phases. This warrants further study of azimuthal shear characteristics in different environments and its potential usefulness in aiding real-time forecasting efforts.

SIGNIFICANCE STATEMENT: This study documents the prolific supercell tornado outbreak that occurred in the southeastern United States on 27–28 April 2011. We associate tornado families with their parent supercells and use a radar-derived database to quantify changes in mesocyclone strength. We show that a variety of supercell evolutionary paths occurred during the event that were somewhat distinct based on where and when each supercell initiated. We also find significant differences between supercell intensity, characterized using azimuthal shear as a measure of mesocyclone strength, during nontornadic periods as opposed to the 30-min window prior to tornadogenesis. These findings are relevant for both researchers and operational forecasters and motivate future work to better understand relationships and processes influencing supercells and their background environments.

1. Introduction

One of the most violent tornado outbreaks ever recorded in the United States impacted the Southeast, Midwest, and East Coast regions on 26–28 April 2011 (Knupp et al. 2014, hereafter K14). According to the Storm Prediction Center (SPC) "One Tornado" database (ONETOR;[1] Schaefer and Edwards 1999; Edwards et al. 2021), from 1200 UTC 26 April to 1200 UTC 29 April, an estimated 300 tornadoes impacted 19 states, resulting in 318 direct tornado-related fatalities (Fig. 1). Of those 318 fatalities, 237 occurred in Alabama, 31 each in Mississippi and Tennessee, 15 in Georgia, and 4 in Virginia. Of the 300 tornadoes, 33 had pathlengths exceeding 40 km (25 mi.), 8 had pathlengths exceeding 80 km (50 mi.), and 3 had pathlengths exceeding 160 km (100 mi.). In total, 64 tornadoes were rated strong (EF2–EF3), and 15 were rated violent (EF4–EF5) on the enhanced Fujita (EF) scale (WSEC 2006).

The April 2011 super outbreak consisted of numerous rounds of tornadic storms. The evolution and interdependence of these convective episodes are described in Chasteen and Koch (2022a,b, hereafter CK22a and CK22b). However, the most impactful tornadic episode commenced across the Southeast around midday on 27 April and continued into the evening, slowly diminishing during the middle of the night and predawn of 28 April along the East Coast. This episode consisted of numerous classic supercell thunderstorms producing long-tracked, intense tornadoes (K14).

Despite the historic nature of this round of supercells, efforts to understand their evolution, including their early morphology,

---

[1] Accessible online at https://www.spc.noaa.gov/wcm/.

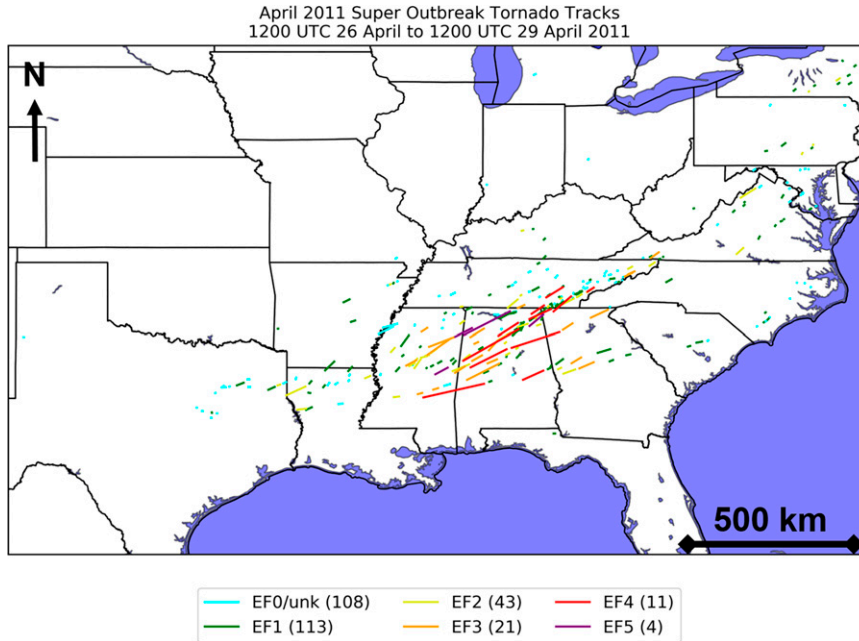*Corresponding author*: Anthony W. Lyza, anthony.lyza@noaa.gov

FIG. 1. Overview map of all 300 tornadoes during 1200 UTC 26 Apr–29 Apr 2011. Note that these statistics differ slightly from the SPC database through the correction process that is described in section 2a and the appendix.

their longevity, and how each tornado family evolved, have been limited in geographic area (e.g., NWS Jackson MS 2021) or to a selection of a few supercells (e.g., K14). To date, no systematic effort has been undertaken to understand the full evolution of these supercells and tornado families, akin to the mappings that were completed for the Palm Sunday 1965 tornado outbreak in the Midwest (Fujita et al. 1970) or the 3 May 1999 tornado outbreak in Oklahoma (Thompson and Edwards 2000).
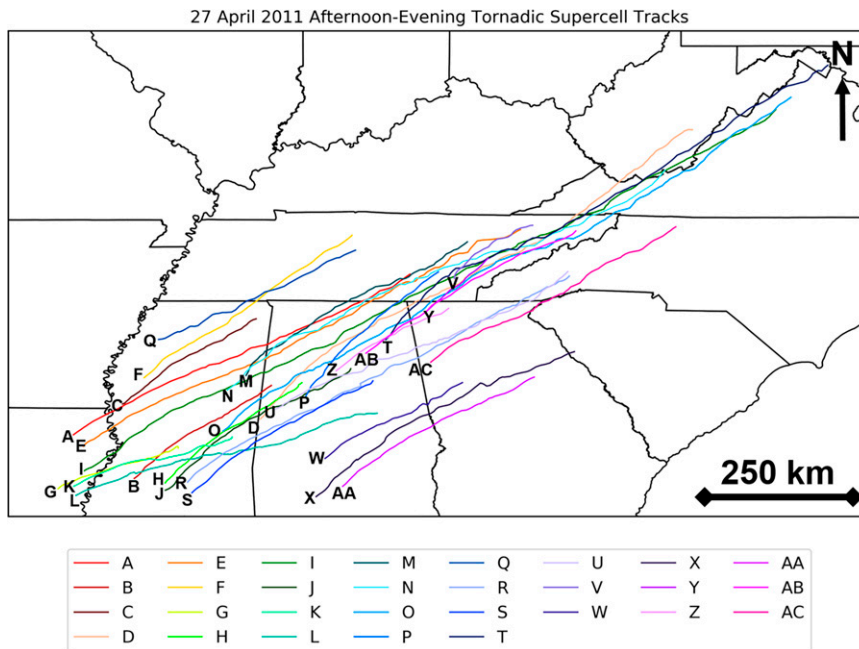

FIG. 2. Overview map of the tracks of the 29 supercells associated with the primary round of destructive tornadoes between midday 27 Apr and the predawn of 28 Apr 2011. The tracks were determined by using a three-point average of maximum Z_h locations centered on each analysis time. Note that these storm tracks do not include any cells associated with the "midday QLCS" discussed in K14 (also discussed in CK22a as "QLCS2").
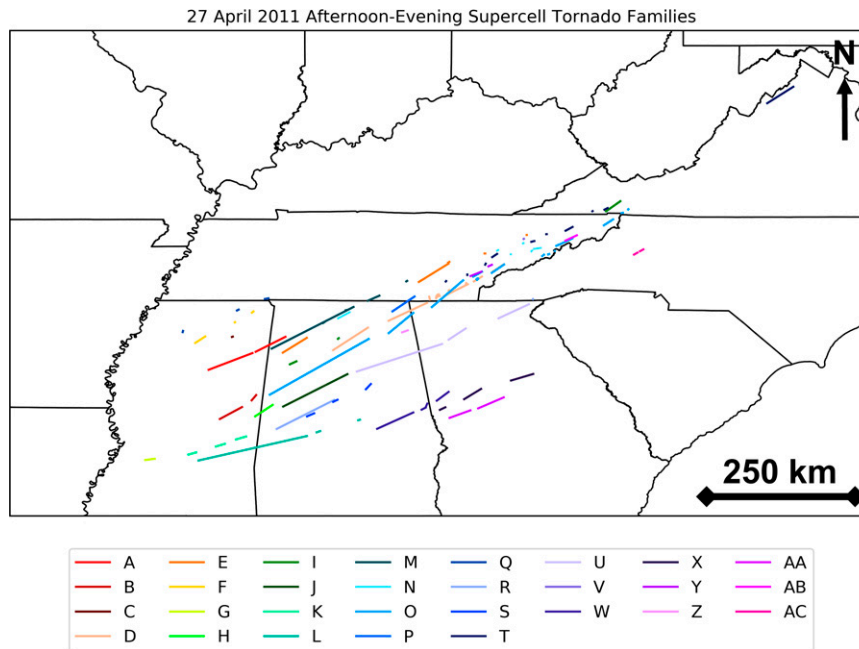
FIG. 3. Overview map of the 102 tornadoes associated with the 29 supercells highlighted in Fig. 2, color coded by parent supercell.

An event the magnitude of 27–28 April 2011 is worthy of not only the documentation of the parent storms and tornadoes but also analysis of their characteristics. Doppler radar is the most commonly used platform for diagnosing real-time tornado potential in a given storm (e.g., Thompson et al. 2017) and estimating the intensity of a tornado associated with a supercell, if one is occurring (e.g., Smith et al. 2015, 2020a,b; Gibbs 2016; Cohen et al. 2018; Gibbs and Bowers 2019). Rotational velocity (V_{ROT}), defined as half the difference value between maximum and minimum radial velocities in a Doppler rotational couplet signature, is a commonly used metric for assessing potential tornado intensity, with the polarimetric tornadic debris signature (TDS; Ryzhkov et al. 2005) becoming increasingly popular since the upgrade of the Weather Surveillance Radar-1988 Doppler (WSR-88D) network to dual-polarization technology.

Recently, the use of Multi-Radar Multi-Sensor (MRMS; Miller et al. 2013; Smith et al. 2016) products, which merge data from multiple radars, satellites, and other observing networks, has proliferated across the National Weather Service (NWS). The Multi-Year Reanalysis of Remotely Sensed Storms (MYRORSS; Williams et al. 2020, 2022) dataset employs an MRMS framework to output numerous radar-derived variables, with velocity-based products output at 0.005° latitude and longitude (approximately 500 m) horizontal grid spacing at 5-min temporal resolution from WSR-88D data from 1998 to 2011. Among the MYRORSS outputs are low-level (0–3-km) and midlevel (3–6-km) azimuthal shear (hereafter AzShear) products (Smith and Elmore 2004; Miller et al. 2013; Mahalik et al. 2019; Williams et al. 2022), which are derived to diagnose the rotational flow in the Doppler velocity field through a linear least squares derivative. The

0–3- and 3–6-km values represent the maximum observed AzShear values within that depth at a given horizontal grid point over a 5-min period from any radar included in the merged analysis, with each timestamp representing the end of a 5-min data merging period (Smith et al. 2016; Williams et al. 2022). These AzShear products have gained popularity in the NWS, particularly as a way to estimate preliminary tornado tracks in the immediate aftermath of a high-impact event (Karstens et al. 2016).

In this study, we use the AzShear products in tandem with observed tornado occurrences to analyze the tracks of 29 supercells that occurred during the 27–28 April 2011 tornado outbreak. We provide detailed documentation of each supercell's tornado family, evolution, and AzShear characteristics during different time periods. This is important for future studies of supercell evolution and tornado production and shows the utility of the MYRORSS database in analyzing such events (e.g., Flournoy et al. 2022).

2. Data and methods

a. Identification of tornadic supercells and associated families

The goal of this study is to examine the characteristics of the primary episode of supercells of the April 2011 super outbreak. The first step toward this goal was to identify the parent supercells and their associated tornado families. To be included in this analysis, the first tornado from any given supercell must have occurred in either Mississippi, Alabama, Tennessee, Georgia, or North Carolina.[2] This geographical

---

[2] None of the supercells assessed produced tornadoes in South Carolina.

TABLE 1. Overview table of each tornadic supercell and characteristics of their associated tornadoes. Abbreviations are as follows: "ID" = storm identification letter; "Tor No." = sequential number of each tornado associated with each parent supercell; "Tor Start Time" and "Tor End Time" = start and end time of each tornado, respectively; "Dur." = the duration in min of each tornado (with start and end time each counting as one full minute of duration); "PL" = pathlength; "PW" = path width; "EF" = enhanced Fujita scale rating; "Fat." = fatalities; and "Inj." = injuries. Boldface values in the duration, pathlength, path width, EF rating, fatality, and injury columns indicate the maximum observed values for each category, and italicized entries indicate information that differs from official *Storm Data* information, with explanation and justification for changes provided in the appendix. Times from 0000 to 1159 UTC 28 Apr (the outbreak occurred in the central and eastern time zones during daylight saving time: CDT = UTC − 5 h; EDT = UTC − 4 h). "U" in the EF column indicates unknown damage intensity, and "unk" elsewhere denotes unknown or missing data. The storm end time occurred either (a) when the midlevel mesocyclone dissipated based on radial velocity presentations (clear inbound–outbound cyclonic peaks in radial velocity above 2 km ARL) or (b) when the storm merged with other convection and lost discrete-supercell characteristics.

ID	First 40-dBZ-echo time (UTC)	Storm end time (UTC)	Tor No.	Counties	Tor start time (UTC)	Tor end time (UTC)	Dur. (min)	PL (km)	PW (m)	EF	Fat.	Inj.
A	1647	2346	1	Webster–Calhoun–Chickasaw–Monroe, MS	1948	2038	51	82.80	1210	3	4	25
			2	Monroe–Itawamba MS–Marion–Franklin, AL	2042	2123	50	59.71	1210	**5**	23	137
B	1657	2041	1	Neshoba–Kemper–Winston–Noxubee, MS	1930	2000	31	45.51	820	**5**	3	6
			2	Noxubee, MS	2018	2029	12	13.39	460	1	0	0
C	1711	2035	1	Pontotoc, MS	1959	2002	4	1.64	70	0	0	0
D	1716	0428	1	Cullman–Morgan–Marshall, AL	1940	2038	59	75.45	800	4	6	48
			2	Jackson–DeKalb AL–Dade–Walker, GA	2101	2157	57	75.61	1150	4	14	*unk*
			3	Hamilton, TN	2203	2208	6	6.12	110	1	0	0
			4	Hamilton, TN	2212	2213	2	0.16	60	0	0	0
			5	Hamilton, TN	2213	2219	7	6.44	80	1	0	0
			6	Hamilton, TN	2214	2221	8	5.79	180	1	0	0
			7	Bradley–Polk–McMinn, TN	2228	2302	35	44.98	230	2	4	0
			8	Bradley, TN	*2235*	*2237*	3	1.61	50	0	0	0
			9	McMinn, TN	2300	2302	3	3.70	50	0	0	0
			10	Monroe, TN	2308	2318	11	16.90	180	2	0	1
			11	Monroe, TN	2310	2321	12	18.35	180	1	0	0
			12	Monroe–Blount, TN	2331	2345	15	23.26	1210	4	0	0
E	1719	0314	1	Marion–Winston, AL	2210	2247	38	51.24	1210	3	0	25
			2	Sequatchie–Bledsoe–Rhea, TN	*0106*	*0141*	36	64.63	800	4	4	12
			3	Sequatchie, TN	*0108*	*0115*	8	7.24	230	2	0	0
			4	Rhea, TN	*0138*	*0143*	6	2.41	70	1	0	0
			5	Knox, TN	0228	0229	2	1.61	50	0	0	0
			6a	Hamblen, TN	0318	0319	2	0.48	50	0	0	0
F	1724	2150	1	Lafayette, MS	1836	1852	17	21.84	400	3	0	8
			2	Union, MS	1928	1929	2	0.64	20	0	0	0
			3	Alcorn, MS	1950	1956	7	3.73	50	0	0	0
G	1747	2112	1	Copiah–Hinds, MS	2011	2024	14	16.83	400	2	0	2
H	1805	2204	1	Kemper MS–Sumter–Pickens, AL	2047	2115	29	38.21	970	3	0	2
I	1819	0836	1	Fayette, AL	2306	2314	9	12.81	800	3	0	0
			2	Cullman, AL	0009	0013	5	1.92	90	0	0	0
			3	Washington–Smyth, VA	0501	0520	20	31.59	1210	3	3	50
J	1823	2321	1	Greene–Tuscaloosa–Jefferson, AL	2143	2314	92	129.84	**2380**	4	64	**1500**
K	1847	2250	1	Smith, MS	2127	2138	12	14.27	400	3	0	0
			2	Newton, MS	2208	2222	17	16.53	400	3	0	0
			3	Lauderdale, MS	2245	2259	15	18.54	90	0	0	0
L	1915	0319	1	Smith–Clarke–Jasper MS–Choctaw–Sumter–Marengo–Perry, AL	2242	0135	**174**	196.40	960	4	7	17
			2	Perry, AL	0150	0153	4	6.82	90	1	0	0
			3	Chilton, AL	0248	0250	3	3.07	50	0	0	1
M	1917	0019	1	*Marion–Franklin–Lawrence–Morgan–Limestone–Madison, AL*	*2005*	*2150*	106	*164.15*	2010	**5**	**71**	*unk*
			2	*Lawrence, AL*	*2112*	*2117*	6	*7.56*	*unk*	*U*	*0*	*0*
			3	Madison, AL	2140	*2142*	3	2.29	70	1	0	0
			4	*Lincoln–Franklin, TN*	*2208*	*2240*	33	*21.52*	*400*	*3*	*0*	*0*
			5	Grundy, TN	2300	2301	2	1.87	50	0	0	0

TABLE 1. (*Continued*)

ID	First 40-dBZ-echo time (UTC)	Storm end time (UTC)	Tor No.	Counties	Tor start time (UTC)	Tor end time (UTC)	Dur. (min)	PL (km)	PW (m)	EF	Fat.	Inj.
N	1924	0420	1	Limestone–Madison, AL	2153	2207	15	23.53	70	1	0	0
			2	Knox, TN	0057	0058	2	1.61	50	1	0	0
			3	Sevier, TN	0106	0107	2	0.80	50	0	0	0
			4	Jefferson, TN	0124	0125	2	1.29	50	0	0	0
			5	Sevier–Jefferson, TN	0131	0133	3	1.77	180	0	0	0
			6	Cocke, TN	0133	0148	16	11.43	140	1	0	0
O	1928	0820	1	Pickens–Tuscaloosa–Fayette–Walker–Cullman–Blount–Marshall, AL	2040	2256	137	**205.67**	1290	4	13	54
			2	DeKalb AL–Dade, GA	2319	2355	37	58.95	1210	**5**	25	*unk*
			3	Catoosa GA–Hamilton–Bradley–Polk–McMinn, TN	0015	0107	53	77.25	730	4	20	335
			4	Monroe, TN	0118	0119	2	1.45	50	0	0	0
			5	Monroe, TN	0120	0131	12	17.70	180	1	0	0
			6	Monroe, TN	0122	0124	3	2.82	50	0	0	0
			7	Monroe–Blount, TN	0135	0150	16	27.20	400	2	0	0
			8	Cocke, TN	0232	0234	3	3.86	40	0	0	0
			9	Cocke, TN	0237	0238	2	1.93	140	1	0	0
			10	Madison, NC	0245	0246	2	0.11	50	0	0	0
			11	Greene, TN	0247	0249	3	3.70	270	0	0	0
			12	Greene–Washington, TN	0251	0308	18	25.43	1370	3	6	33
			13	Johnson, TN	0345	0356	13	19.31	230	2	2	0
			14	Washington, VA	0405	0406	2	0.80	180	1	0	0
			15	Smyth, VA	0413	0414	2	0.66	270	1	0	0
P	1934	2308	1	Jackson AL–Marion, TN	2205	2231	27	48.67	1210	4	1	0
Q	1954	2347	1	Panola, MS	2017	2022	6	2.54	20	0	0	0
			2	Tippah, MS	2140	2142	3	3.43	90	1	0	0
			3	Hardin, TN	2211	2215	5	6.18	180	2	0	2
R	2005	0526	1	Greene–Hale–Bibb, AL	2230	2355	86	116.08	1610	3	7	50
			2	Macon, NC	0431	0432	2	0.39	30	0	0	0
S	2028	0131	1	Hale–Bibb, AL	2350	0002	13	13.87	270	1	0	0
			2	Bibb–Shelby, AL	0032	0038	7	8.71	50	1	0	0
			3	Shelby–Talladega, AL	0115	0124	10	13.82	180	1	0	0
T	2134	0730	1	Meigs, TN	2307	2308	2	1.21	100	0	0	0
			2	McMinn, TN	2335	2336	2	1.13	20	0	0	0
			3	Loudon, TN	0000	0002	3	1.61	50	0	0	0
			4	Blount, TN	0009	0015	7	10.46	180	0	0	0
			5	Jefferson, TN	0046	0050	5	5.31	50	0	0	0
			6	Greene, TN	0107	0108	2	0.80	60	0	0	0
			7	Greene–Washington, TN	0129	0137	9	14.16	140	2	0	0
			8	Washington, VA	0204	0205	2	0.80	50	0	0	0
			9	Washington, VA	0213	0217	5	6.28	90	1	0	0
			10	Rockingham–Shenandoah, VA	0612	0641	30	53.93	370	2	0	0
U	2148	0409	1	Jefferson–St. Clair–Calhoun–Etowah–Cherokee AL–Polk–Floyd–Bartow, GA	2328	0115	108	156.64	1610	4	22	85
			2	Bartow–Cherokee–Pickens, GA	0120	0149	30	37.10	800	3	0	25
			3	Lumpkin–White–Habersham–Rabun, GA	0230	0316	47	59.53	820	3	1	1
V	2335	0111	1	Jefferson, TN	0111	0112	2	0.48	50	0	0	0
W	2350	0326	1	Elmore–Tallapoosa–Chambers, AL	0112	0209	58	71.10	800	4	7	30
			2	Chambers, AL	0219	0228	10	8.43	140	1	0	0
			3	Chambers, AL	0229	0238	10	8.06	90	1	0	0
			4	Troup–Heard–Coweta, GA	0250	0310	21	27.39	90	1	0	1
X	2355	0638	1	Troup, GA	320	0330	11	10.83	400	2	0	6
			2	Meriwether–Spalding–Henry, GA	0359	0428	30	34.89	800	3	2	0
			3	Newton–Morgan–Greene, GA	0511	0540	30	40.57	800	1	0	0
Y	0025	0149	1	McMinn–Monroe, TN	0125	0136	12	20.12	180	1	0	1

TABLE 1. (*Continued*)

ID	First 40-dBZ-echo time (UTC)	Storm end time (UTC)	Tor No.	Counties	Tor start time (UTC)	Tor end time (UTC)	Dur. (min)	PL (km)	PW (m)	EF	Fat.	Inj.
			2	Blount, TN	0143	0149	7	6.12	90	0	0	0
Z	0048	0309	1	DeKalb, AL	0205	0210	6	10.41	230	2	0	0
AA	0054	0605	1	Harris–Meriwether–Upson, GA	0355	0424	30	39.43	1210	2	0	0
			2	Pike–Lamar–Monroe–Butts, GA	0438	0517	40	49.60	970	3	2	22
AB	0100	0501	1	Greene–Washington, TN	0440	0456	17	21.89	910	3	2	70
AC	0244	0832	1	Caldwell, NC	0722	0730	9	7.16	90	1	0	1
			2	Alexander, NC	0733	0740	8	6.95	70	1	0	0

[a] Tornado E6 occurred soon after supercell E lost clearly identifiable supercellular characteristics on radar. It is excluded in the AzShear analyses provided in this manuscript but included in this table for completeness.

limitation was imposed to eliminate supercells that were responsible for weaker tornadoes across the Mid-Atlantic and northeastern United States. Tornado information from the ONETOR database was sorted temporally, and tornadoes that fell outside of the period spanning 1200 UTC 27 April–1200 UTC 28 April were excluded from analysis. The start points of the remaining tornadoes were then overlaid in the GR2Analyst software package,[3] which included displaying start time, tornado dimension, and magnitude information. Analysis of level-2 radar data in GR2Analyst was chosen over the MYRORSS data to allow for inspection of the raw, higher-resolution level-2 reflectivity data instead of the MYRORSS reflectivity products, which are processed at approximately 1-km horizontal grid spacing (Williams et al. 2022).

Upon overlaying the tornado information in GR2Analyst, an iterative process was then undertaken to identify the parent supercell responsible for each tornado and group the tornadoes into their respective families by overlaying data from the proximity WSR-88D radars. During this process, obvious errors in the ONETOR dataset, including time zone errors, start/end time inconsistencies, and previously documented track information errors, were noted and corrections were applied to the tornado track information prior to performing the azimuthal shear analyses described in section 2b. Justification for the corrections applied to the tornado track information are provided in the appendix.

Once all of the tornadoes from the afternoon supercells were grouped into their respective families, the life cycle of each supercell was then documented. The procedure for supercell life cycle documentation consisted of tracking each parent supercell during the period from its first continuous 40-dBZ reflectivity (Z_h) echo (hereafter convection initiation or CI; e.g., Wilson and Roberts 2006; Weckwerth et al. 2019; Davenport 2021) to the last readily apparent midlevel mesocyclone. During that period, the latitude, longitude, and altitude of the maximum Z_h echo value per volume from the closest functioning WSR-88D radar was recorded. Finally, a letter identifier was assigned to each parent tornadic supercell

based on the time of CI, and storms that initiated at the same time were assigned identifiers from north to south. Storms retained the same letter identifiers if they underwent cyclic mesocyclogenesis with the new mesocyclone evolving from the same discrete radar echo as the previous mesocyclone, but a new letter identifier was applied if the new mesocyclone originated outside of the original discrete radar echo. Characteristics of these supercells and their tornado families are presented in section 3.

b. MYRORSS azimuthal shear analysis

The MYRORSS database was used to assess low-level (0–3-km) and midlevel (3–6-km) mesocyclone intensity changes during the lifespans of the identified tornadic supercells. To obtain time series of 0–3- and 3–6-km AzShear for each tornadic supercell, the latitude and longitude data for each supercell obtained in the analysis described in section 2a were used. Data points at 2-h increments were used to define a storm motion vector from each initial latitude–longitude point within each increment, and each storm was tracked for that 2-h period at 5-min increments corresponding to the resolution of the MYRORSS files. The selection of 2 h as the increment for performing this analysis was to facilitate manual quality control checks on the AzShear maxima tracing during the analysis of each of the often very long-lived supercells. These storm motion estimates were only used to trace the AzShear maxima within each 2-h interval and not for any other analysis presented in this study. To account for errors between maximum Z_h location, mesocyclone location, and mesocyclone tilt within each storm, a radius of 20 km was used at each time step to "search" for the peak AzShear value. These analyses were replicated at successive 2-h intervals until the entire timespan of each supercell was analyzed.

Upon completing the analysis of each storm, a quality control process was performed to ensure accurate identification of the analyzed supercell's primary mesocyclone by creating a cursory map of the AzShear maxima at all analysis times during the supercell life cycle. Suspected errors in AzShear maxima locations were investigated by manually comparing the maximum location to radar data from the closest WSR-88D.

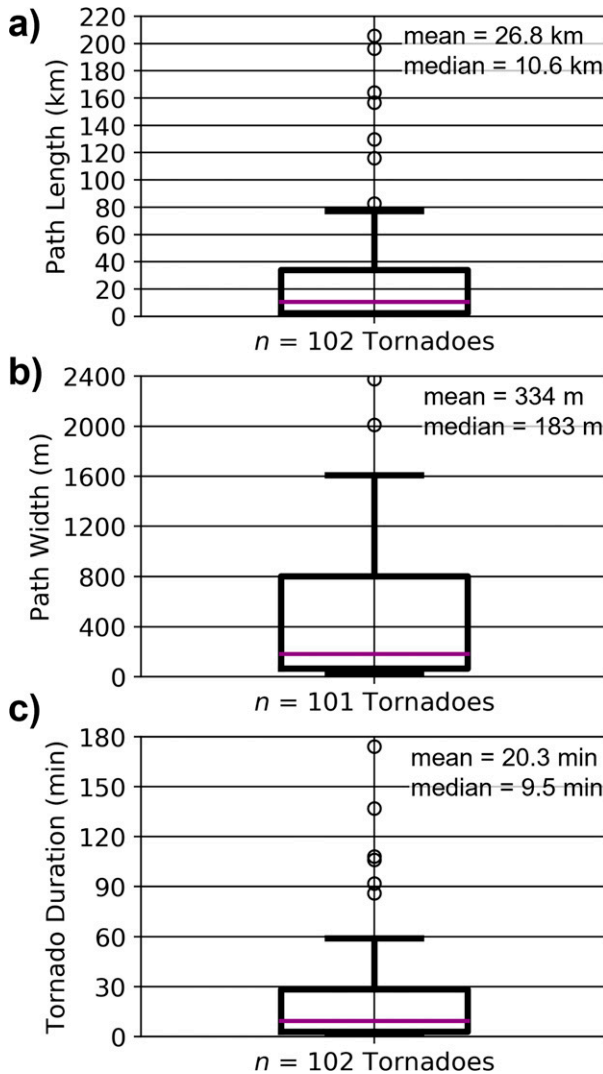[3] Accessible online at http://grlevelx.com/gr2analyst_2/.

FIG. 4. Box-and-whisker plots of (a) pathlength, (b) path width, and (c) tornado duration for *n* number of tornadoes across the primary round of 27–28 Apr 2011 supercells. The purple line indicates the median for each sample, each box represents the middle 50% of observations, the interquartile range (IQR) is given by the range of each box, each bottom whisker extends to either the minimum observed value or the value given by the bottom of the box −(1.5 × IQR), and each top whisker extends to either the maximum observed value or the value given by the top of the box +(1.5 × IQR) Circles denoted outliers beyond the whiskers. Path width has one less observation because of the unknown width of tornado M2. Note that all box-and-whisker plots that follow are designed using the same methodology.

FIG. 5. Box-and-whisker plot for $\Delta t_{\text{CI–TG}}$ for the 29 tornadic supercells in the Southeast on 27–28 Apr 2011.

was completed, tornado information for each analysis time during each supercell life cycle was added, including whether a tornado was occurring and, if so, what the EF scale rating of the tornado was. If multiple tornadoes were ongoing in association with the same supercell at the analysis time, the highest EF-scale rating was recorded. Because most tornado tracks did not have along-track intensity information in the NWS Damage Assessment Toolkit, and several that did had insufficient data points or data points that were inconsistent with storm survey summary narratives, only the maximum EF rating along each tornado track was recorded.

After merging the AzShear and tornado data, statistics were compiled to compare AzShear attributes to tornadic characteristics of each storm. AzShear values were designated as either nontornadic (no tornado ongoing, and none forming within 30 min after the observation), pre-tornadic (no tornado ongoing but tornadogenesis—defined by tornado start time— observed within 30 min after the observation), or tornadic (tornado ongoing at or within the 5-min data merging period prior to the timestamp of the observation). Because of the aforementioned lack of information regarding along-track tornado intensity variations, comparison of tornado damage intensity to AzShear was limited to the maximum values of damage intensity and the mean and maximum AzShear during each tornado life cycle. To ensure statistical independence, two tornadoes occurring simultaneously within any 5-min data-merging
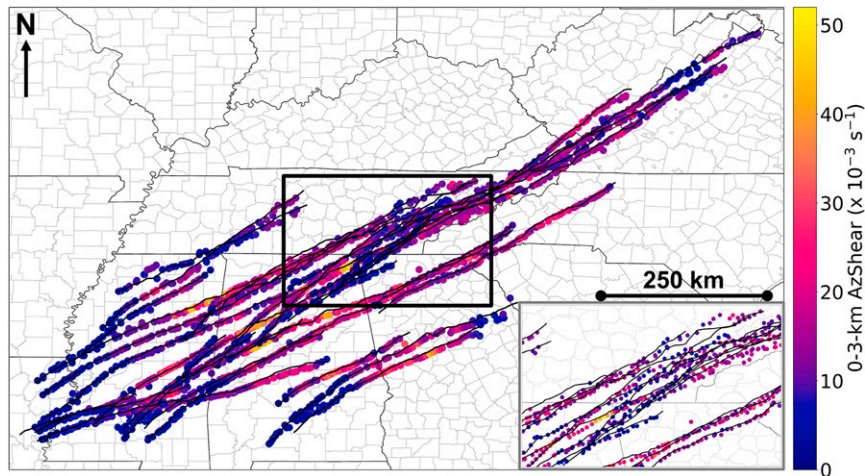
If the location of the AzShear maximum was found to be in error (e.g., rotation associated with a different nearby cell within the 20-km tracking radius was attributed to the analyzed supercell), the tracking was performed again for the erroneous time period(s) using manually estimated first-guess mesocyclone locations from the WSR-88D data in GR2Analyst and a 5-km search radius. Once AzShear maxima identification

FIG. 6. Maximum Z_h tracks (as in Fig. 3; black lines) and individual 0–3-km AzShear observations (markers) for all 29 supercells analyzed in this study. The inset is zoomed in on the area highlighted by the box.

time period were lumped into one "event" and assigned the highest rating among the combined tornadoes.[4] Aside from the maximum AzShear values during each tornadic period, individual AzShear values were not statistically analyzed due to significant autocorrelation (persistence) across observations. Instead, mean values of AzShear for every nontornadic, pre-tornadic, and tornadic period within each storm's life cycle were computed. These mean values were then used to compare AzShear statistics for nontornadic, pre-tornadic, and tornadic periods to reduce the impact of persistence in the analysis, as opposed to using the individual AzShear observations.

c. Environmental analyses

Background mesoscale environments in the vicinity of the tornadic supercells were characterized using analyses from the NOAA/NCEP operational RUC (Rapid Update Cycle) hourly assimilation system and forecast model (Benjamin et al. 2004a,b). This model features a 13-km horizontal grid spacing; convection is not explicitly resolved and is implicitly represented via a cumulus parameterization. We use these analyses to diagnose differences in the background environments of different clusters of storms, which are then linked to differences in supercell evolutionary characteristics.

3. Supercell and tornado family classification and characteristics

A total of 29 tornadic supercells (Fig. 2) were responsible for 102 tornadoes (Fig. 3) during the primary destructive supercell

episode of the 26–28 April 2011 super outbreak (Table 1). The casualties and damage exacted by these supercells were tremendous. All 15 EF4–EF5 tornadoes, 28 of 64 (43.8%) EF2–EF3 tornadoes, and 313 of the 318 fatalities (98.4%) associated with the outbreak[5] were associated with these supercells. Of the 313 fatalities, 201 (64.2%) were associated with the three deadliest tornado families: 71 fatalities (22.7%) with supercell M, all from the Hackleburg–Phil Campbell–Tanner–Harvest, Alabama, EF5 tornado; 66 (21.1%) with supercell O from five separate tornadoes; and 64 (20.4%) with supercell J, all associated with the Tuscaloosa–Birmingham, Alabama, EF4 tornado. Over half of the supercells produced deadly tornadoes (16 of 29; 55.2%), and 23 of the 102 tornadoes (22.5%) produced fatalities. Of the 29 tornadic supercells, 23 (79.3%) produced at least one significant (EF2 or greater) tornado during their lifespans. The three most prolific supercells (by tornado count) were supercell O (15 tornadoes; 14.7% of tornadoes observed in the supercell round), supercell D (12; 11.8%), and supercell T (10; 9.8%). Only two supercells produced multiple violent-rated tornadoes: supercell D (the Cullman, Alabama EF4; the Pisgah, Alabama–Trenton, Georgia EF4; and the Great Smoky Mountains National Park, Tennessee EF4) and supercell O (the Cordova, Alabama EF4; the Rainsville, Alabama EF5; and the Ringgold, Georgia–Apison, Tennessee EF4).

Characteristics of tornado pathlength, width, and duration are summarized in Fig. 4. The differences between the means and medians indicate that the mean values were skewed by a number of particularly large, long-tracked, and long-lived tornadoes. Notably, the longest-duration tornado (L1) formed at 2242 UTC and dissipated at 0135 UTC, persisting for 2 h 54 min, with a pathlength of 196.40 km (122 mi.) and a mean

---

[4] For example, an EF4 tornado occurring from 0106 to 0141 UTC and an EF1 tornado occurring from 0138 to 0143 UTC with an AzShear data point at 0142 UTC would be merged into one EF4 "event" spanning from 0106 to 0143 UTC, and the highest 0–3- and 3–6-km AzShear values during that time frame would be applied as the maximum AzShear values for the entire "event."

[5] Defined as 1200 UTC 26–29 April.

TABLE 2. Mean and median values of 0–3- and 3–6-km AzShear for all nontornadic, pre-tornadic, and tornadic observations. The number of observations per category is given by n.

Value	Nontornadic periods (n = 68)	Pre-tornadic periods (n = 73)	Tornadic periods (n = 88)
Mean 0–3-km AzShear ($\times 10^{-3}$ s^{-1})	10.4	14.2	17.5
Median 0–3-km AzShear ($\times 10^{-3}$ s^{-1})	10.2	14.1	16.7
Mean 3–6-km AzShear ($\times 10^{-3}$ s^{-1})	9.5	13.6	14.8
Median 3–6-km AzShear ($\times 10^{-3}$ s^{-1})	9.4	13.0	14.5

forward speed of 18.8 m s^{-1} (42 mph). This duration rivals the infamous 1925 TriState Tornado event, which had a likely continuous pathlength of 280 km (174 mi.) and an estimated mean forward speed of 26.4 m s^{-1} (59 mph; Johns et al. 2013), leading to a duration of 2 h 57 min. Additionally, analysis of the time elapsed between CI and first tornadogenesis event with each tornadic supercell (hereafter $\Delta t_{\text{CI–TG}}$) shows a substantial range in time over which the supercells matured prior to tornadogenesis (Fig. 5). The median $\Delta t_{\text{CI–TG}}$ was 2 h 31 min, with the middle 50% of $\Delta t_{\text{CI–TG}}$ values ranging from 1 h 23 min to 3 h 19 min, a minimum of 23 min, and a maximum of 4 h 51 min. Regional variability in the early evolution and maturation of supercells is discussed in section 5.

4. Bulk azimuthal shear analysis

As discussed in section 2b, individual AzShear observations (e.g., Fig. 6) were lumped into nontornadic, pre-tornadic, and tornadic periods to minimize the impact of autocorrelation across observations. A clear increase is evident in both 0–3- and 3–6-km AzShear from nontornadic to pre-tornadic and pre-tornadic to tornadic phases (Table 2 and Fig. 7). While there is overlap between the distributions, Welch's

FIG. 7. Box-and-whisker plots for (a) 0–3- and (b) 3–6-km mean AzShear values for nontornadic, pre-tornadic, and tornadic periods.

t test (Welch 1947) p values indicate that all the mean AzShear differences are statistically significant to >99% confidence ($p < 0.01$) except for the difference in means between pre-tornadic and tornadic 3–6-km mean AzShear, which is statistically significant to 90% confidence ($p = 0.10$).

The combination of tornadoes into "events," as described in section 2b, leads to a total of 88 tornado events for analysis. Of these 88 tornado events, 46 were weak (EF0–EF1) maximum damage intensity, 27 were strong (EF2–EF3), and 15 were violent (EF4–EF5). Comparison of the tornado-mean AzShear values for each intensity category shows a tendency for increasing AzShear with increasing damage intensity (Table 3), albeit with some overlap in the distributions (Fig. 8). Despite the overlap, p values from a series of Welch's t tests indicate >95% confidence that the means of the tornado-mean AzShear values are different for weak versus strong and weak versus violent tornadoes for both 0–3- and 3–6-km AzShear (Table 4). Strong and violent tornado-mean AzShear distribution differences are statistically significant at a >93% confidence level for 0–3-km and at a >98% confidence level for 3–6-km AzShear. A similar relationship is indicated for tornado-maximum AzShear (Table 3), with slightly greater differences between in the distributions (Fig. 9) and p values indicating that the differences in mean 0–3- and 3–6-km tornado-maximum AzShear values are statistically significant at a >95% confidence level for all comparisons (Table 4). The magnitude of mean pre-tornadic AzShear showed little skill in predicting the resulting peak tornado damage intensity (Fig. 10).

Given the known challenges posed to sampling of severe and potentially tornadic storms with increasing range from a radar due to beam broadening and increasing minimum elevation above ground level (e.g., Brown et al. 2005) and the subsequent impacts on warning skill (e.g., Brotzge and Erickson 2010), the relationship between maximum AzShear and maximum tornado damage intensity was further examined to determine if the relationship was impacted by the distance of the tornado-maximum AzShear value observed during each "event" from the nearest operating WSR-88D radar (Fig. 11). Only a weak negative correlation was found between 0 and 3-km maximum AzShear and distance to the closest radar for weak and strong tornado events, each with coefficients of determination (R^2) of 0.16, indicating that the proximity to the closest radar can explain 16% of the variance in tornado-maximum AzShear for weak and strong tornadoes. Similarly weak negative correlations exist for 3–6-km AzShear and weak–strong tornado events, with weak tornado events exhibiting no correlation ($R^2 = 0.05$)
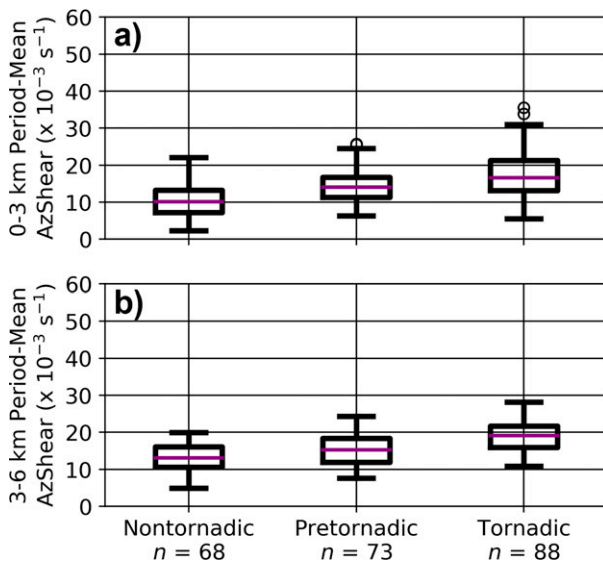
TABLE 3. Mean and median values of maximum 0–3- and 3–6-km tornado-mean and tornado-maximum AzShear for each peak tornado event intensity.

Value	EF0–EF1 (n = 46)	EF2–EF3 (n = 27)	EF4–EF5 (n = 15)
Mean of the 0–3-km tornado-mean/tornado-maximum AzShear ($\times 10^{-3}$ s^{-1})	15.1/16.6	18.5/24.7	22.9/33.3
Median of the 0–3-km tornado-mean/tornado-maximum AzShear ($\times 10^{-3}$ s^{-1})	15.4/16.5	18.0/24.5	22.3/32.7
Mean of the 3–6-km tornado-mean/tornado-maximum AzShear ($\times 10^{-3}$ s^{-1})	13.1/14.5	15.3/19.8	19.1/27.3
Median of the 3–6-km tornado-mean/tornado-maximum AzShear ($\times 10^{-3}$ s^{-1})	13.2/13.7	15.3/17.2	19.2/28.6

and strong tornado events exhibiting weak–moderate correlation ($R^2 = 0.25$). Overall, the maximum AzShear associated with weak and strong tornado events was weakly sensitive to distance to the closest WSR-88D radar in the 27–28 April supercells.

However, the relationships between 0–3- and 3–6-km AzShear maxima and distance to the closest WSR-88D radar for violent tornado events illustrate a different picture. Both 0–3- and 3–6-km maximum AzShear exhibit a strong negative correlation to distance from the nearest WSR-88D radar, with downward-sloping best-fit lines and R^2 values of 0.79 and 0.78, respectively. For both depths of AzShear, the end result is that the difference in maximum AzShear magnitude for weak, strong, and violent tornadoes is greater for events closer to the nearest radar, and difficult to distinguish at farther distances, particularly beyond about 150 km. The strength of the slope and correlation may also explain the larger size of the boxes for maximum AzShear values for violent tornadoes in Fig. 8 given the more widely distributed range of AzShear values, particularly for 0–3-km AzShear, which exhibits a steeper downward slope to its best-fit line than for 3–6-km AzShear.
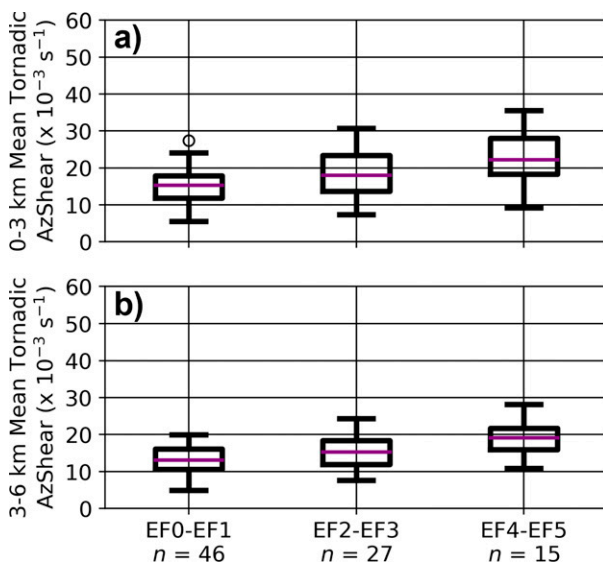
While the tornadic supercells of 27–28 April 2011 represent a large sample size for a single event, they still pose the limitations of having been from one event (Doswell 2007), which happened to be particularly anomalous relative to the broader tornado climatology and comprising a small sample size overall. The results of this study suggest that AzShear can be a useful diagnostic tool in assessing whether a storm is or is not producing a tornado, and if so, how intense the damage associated with that tornado might be. There might also be limited prognostic capability to better anticipate the potential for tornadogenesis within a 30-min period based on background AzShear trends with a given storm. However, to better contextualize these capabilities, additional studies should be conducted on storms in varying or less conducive environments and across different storm modes.

5. Regional differences in supercell characteristics and evolution

a. CI and first tornadogenesis

The data presented in sections 3 and 4 reveal the diversity of morphology among the formidable 27–28 April 2011 supercells. Despite the extreme parameter space detailed in K14 and CK22a and noteworthy examples of high-profile supercells evolving quickly—such as supercell M (the Hackleburg-Phil Campbell EF5 storm) producing an EF5 tornado 48 min after CI—75% of the supercells took 1 h 23 min or longer to produce their first tornado after CI, and 50% took over 2.5 h. A mapping of supercell tracks by $\Delta t_{\text{CI–TG}}$ reveals substantial spatial variability in the time taken for storms to produce their first tornado (Fig. 12). One notable trend is the tendency for the fastest 25% of cases to be clustered across northern Mississippi and northern Alabama. This clustering
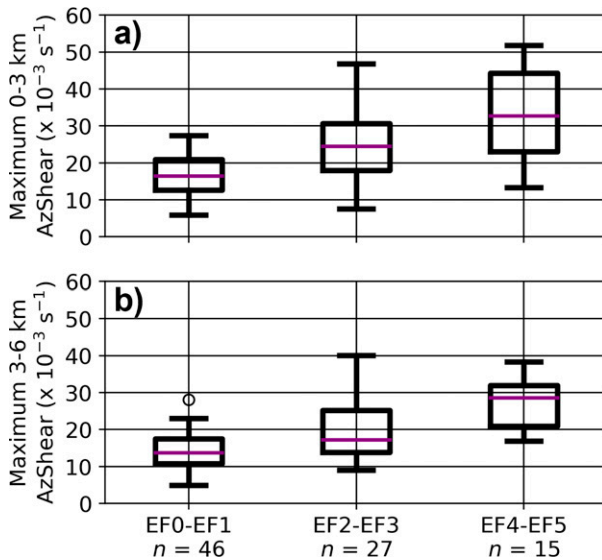

FIG. 8. As in Fig. 7, but for tornado-mean AzShear values during each tornado "event," separated by weak (EF0–EF1), strong (EF2–EF3), and violent (EF4–EF5) maximum tornado damage intensity.

TABLE 4. Welch's t test p values for tornado-mean/tornado-maximum 0–3- and 3–6-km AzShear differences between EF0–EF1 (weak), EF2–EF3 (strong), and EF4–EF5 (violent) damage intensities.

Test	0–3 km	3–6 km
EF0–EF1 vs EF2–EF3 (tornado-mean)	0.017	0.0409
EF0–EF1 vs EF2–EF3 (tornado-maximum)	0.0004	0.0032
EF2–EF3 vs EF4–EF5 (tornado-mean)	0.0633	0.0142
EF2–EF3 vs EF4–EF5 (tornado-maximum)	0.0301	0.0036
EF0–EF1 vs EF4–EF5 (tornado-mean)	0.0012	0.0002
EF0–EF1 vs EF4–EF5 (tornado-maximum)	0.0001	0.0000

FIG. 9. As in Fig. 7, but for tornado-maximum AzShear values during each tornado "event," separated by weak (EF0–EF1), strong (EF2–EF3), and violent (EF4–EF5) maximum tornado damage intensity.

is intriguing given the presence of a thermal boundary zone, described in K14 and CK22a, which initially consisted of two remnant boundaries from the first two quasi-linear convective system (QLCS) episodes that impacted the region during the morning and midday of 27 April before the boundary from the first QLCS became indistinguishable. Such thermal boundaries have been noted as important modulators to tornado risk with supercell thunderstorms (e.g., Maddox et al. 1980; Markowski et al. 1998; Rasmussen et al. 2000; Garner 2012; Boustead et al. 2013; Magee and Davenport 2020).

When accounting for location and time of CI and the spatiotemporal evolution of the thermal boundaries, dryline, and Pacific cold front identified in CK22a and evident in surface analyses of virtual potential temperature (θ_v) from the RUC, the 29 supercells can be stratified into four clusters (shown in Fig. 13):

1) Louisiana Delta (six supercells: A, E, G, I, K, and L);
2) South Mississippi to west-central Alabama (seven supercells: B, H, J, O, R, S, and U);
3) Along or near the thermal boundary zone and into the Great Tennessee Valley of east Tennessee (12 supercells: C, D, F, M, N, P, Q, T, V, Y, Z, and AB); and
4) South Alabama into western Georgia (four supercells: W, X, AA, and AC).

While there was wide temporal variability in $\Delta t_{CI–TG}$ across the full dataset of 29 tornadic supercells, a breakdown of the supercells by their initiation clusters reveals a distinct tendency for supercells forming closer to the thermal boundary zone to mature, develop supercellular characteristics, and produce their first tornadoes faster than supercells forming in regions farther away from the boundary zone (Fig. 14). A
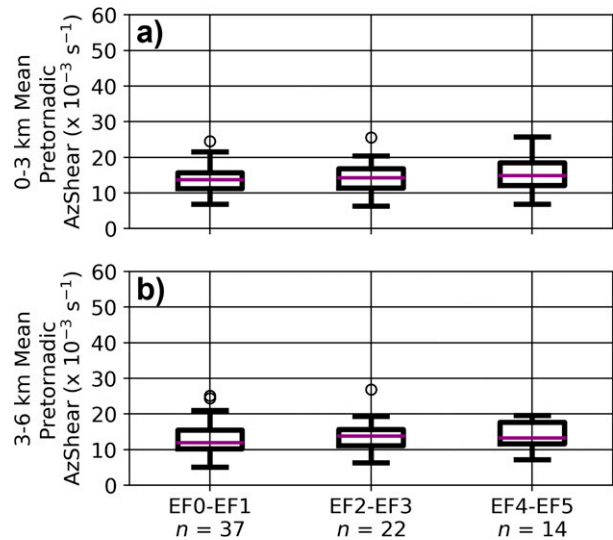
FIG. 10. As in Fig. 7, but for pre-tornadic mean AzShear stratified by resulting maximum tornado damage intensity.

Welch's t test indicates the difference in mean $\Delta t_{CI–TG}$ for the combination of clusters 1, 2, and 4 compared to cluster 3 (Fig. 14b) is statistically significant at the >99% confidence level, with a p value of 0.0045. A similar relationship is also evident for the formation of each supercell's midlevel mesocyclone. Using a 3–6-km AzShear of >0.01 s^{-1} (e.g., Burgess et al. 1975; Smith et al. 2016) for at least three consecutive observations as a threshold for "strong" midlevel mesocyclone development,[6] a clear tendency becomes apparent for supercells forming in cluster 3 (along the boundary zone) to develop strong midlevel mesocyclones faster than those in the clusters south of the boundary zone (Fig. 15a). Furthermore, a moderately strong correlation exists between the time from CI to strong mesocyclogenesis and $\Delta t_{CI–TG}$, with supercells forming in cluster 1 showing a greater elapsed time from strong mesocyclogenesis to tornadogenesis (Fig. 15b).

b. Regional environmental and storm characteristic variability

The mesoscale environment in the vicinity of supercells forming along the boundary zone (i.e., clusters 3a and 3b in Fig. 16) varied substantially from that in the vicinity of supercells in other clusters. The environment near the boundary zone at representative times for CI (i.e., 1800 and 0000 UTC) featured less CAPE, greater CIN, lower LCLs, and much greater SRH than the environments present farther south (Fig. 17). The exceptional low-level SRH in this environment (e.g., near or exceeding 500 m^2 s^{-2} in the 0–1-km layer and >750 m^2 s^{-2} in the 0–3-km layer) and associated amounts of

---

[6] All supercells featured at least one 3–6-km AzShear observation exceeding 0.01 s^{-1}. However, supercells Q and Y did not feature three consecutive observations exceeding 0.01 s^{-1} and are thus excluded from this analysis.
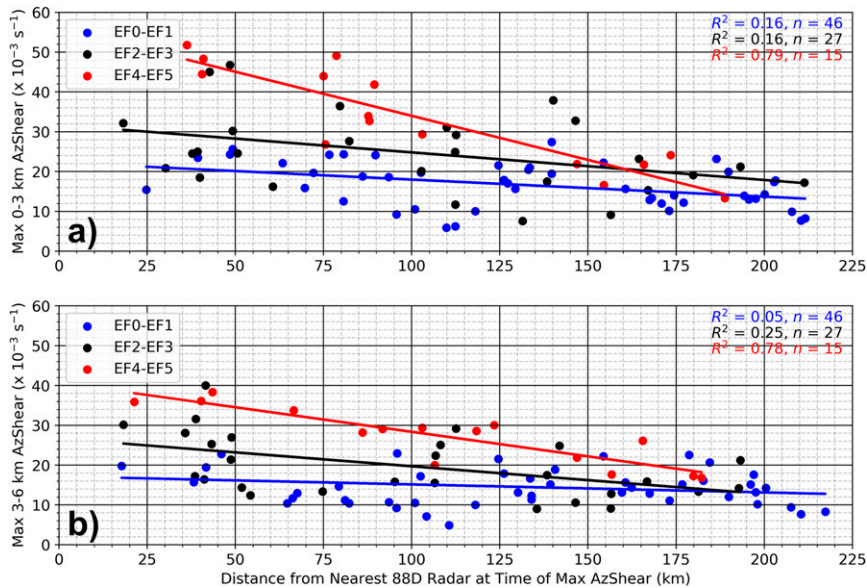
FIG. 11. Scatterplots of (a) 0–3- and (b) 3–6-km tornado-maximum AzShear vs distance from the nearest WSR-88D radar at the time of maximum AzShear for all 88 tornado "events," stratified by weak (EF0–EF1), strong (EF2–EF3), and violent (EF4–EF5) maximum tornado event damage intensity. The lines of best fit, coefficients of determination (R^2), and sample size (n) are provided for reference.

streamwise vorticity (e.g., Davies-Jones 1984; Flournoy et al. 2021) likely contributed to the rapid tornado production within these storms.

While the storms that initiated closer to the boundary zone tended to produce their first tornadoes more quickly than storms in the other initiating clusters, the individual tornadoes they produced tended to be shorter-tracked and narrower *on average* than their counterparts (Fig. 17). This is not readily explained by the small differences between the mesoscale environments in the vicinity of these clusters (Fig. 16). Cluster 3 also had a much lower percentage of significant tornadoes (31.8%) than the other clusters (55.2% combined), despite having more significant tornadoes total than any other cluster (Table 5). However, this cluster was also the most prolific, with 44 of the 102 tornadoes (43.1%) occurring in cluster 3, roughly in line with the percentage of total supercells that
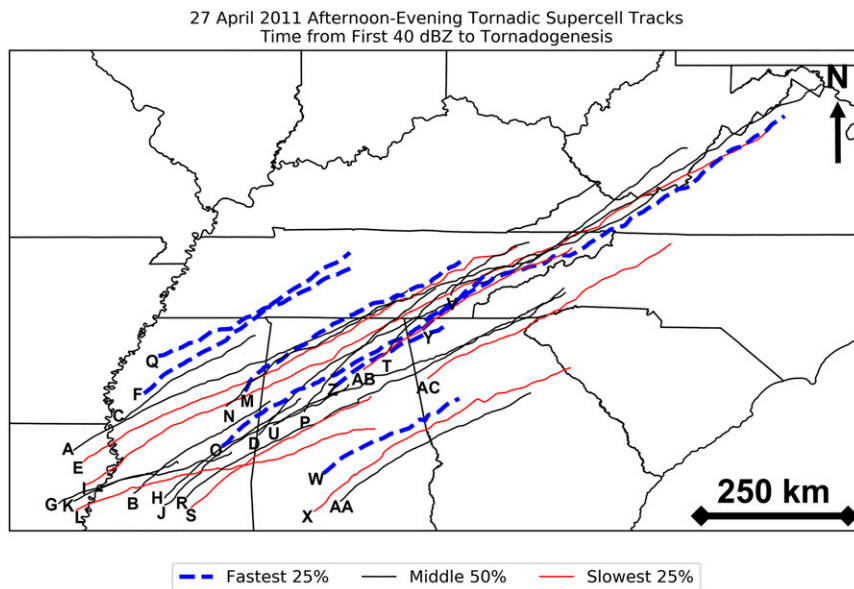
FIG. 12. As in Fig. 2, but with tracks coded by $\Delta t_{\text{CI–TG}}$.
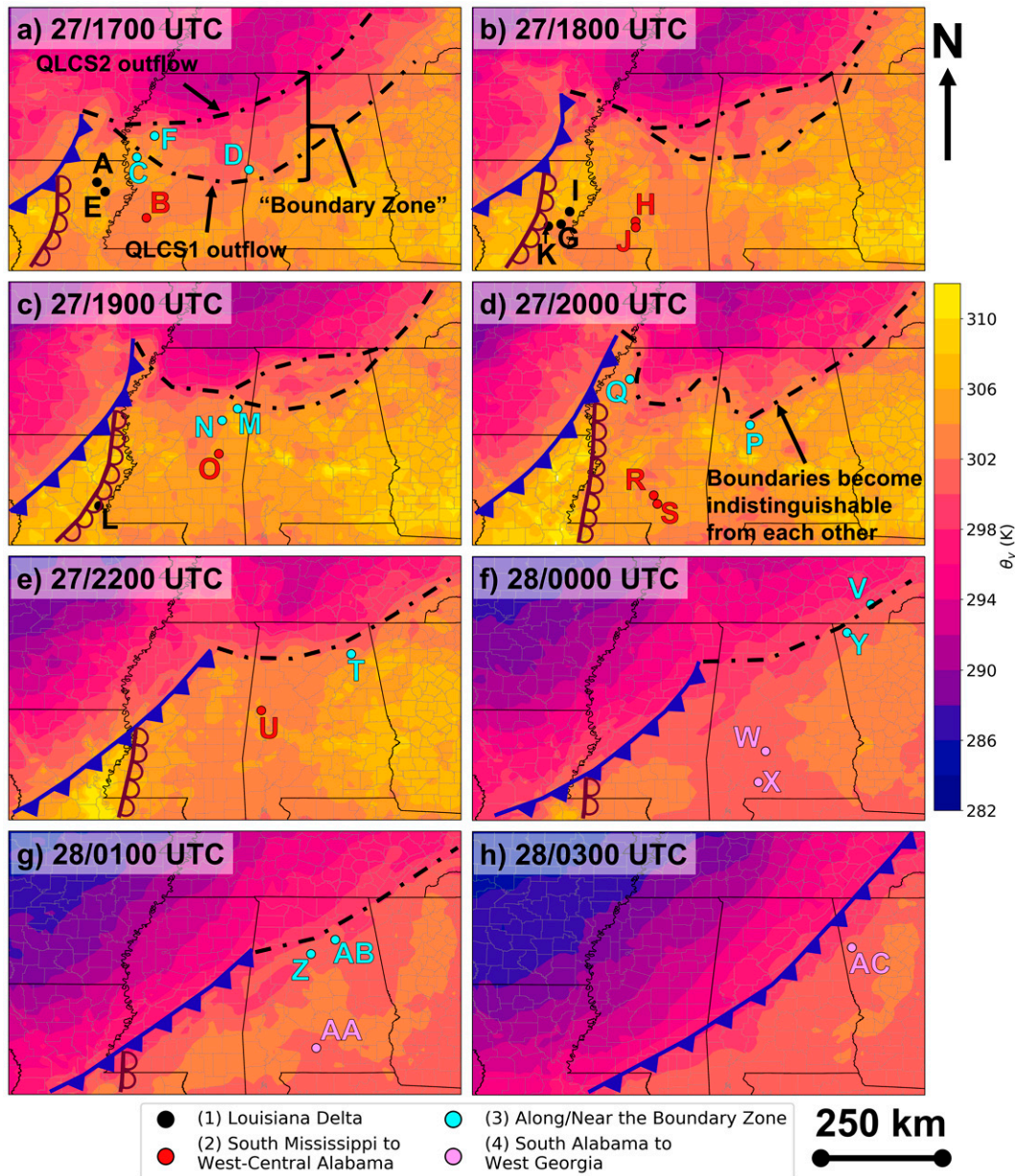
FIG. 13. RUC surface θ_v analyses at (a) 1700 UTC 27 Apr, (b) 1800 UTC 27 Apr, (c) 1900 UTC 27 Apr, (d) 2000 UTC 27 Apr, (e) 2200 UTC 27 Apr, (f) 0000 28 Apr, (g) 0100 UTC 28 Apr, and (h) 0300 UTC 28 Apr. CI locations for supercells that initiated within ±30 min of each analysis time are shown, coded by initiation cluster. The locations of the remnant outflow boundaries from the first two QLCSs (black dotted–dashed), dryline (brown scalloped line), and Pacific cold front (blue line with triangles) are provided for reference. Analyses at 2100 UTC 27 Apr, 2300 UTC 27 Apr, and 0200 UTC 28 Apr are omitted because no supercells initiated with the ±30 min windows surrounding those analysis times.

were initiated in cluster 3 (12 of 29 or 41.4%). Calculation of the destruction potential index[7] (DPI; Thompson and Vescio 1998) of each tornado and summation of those values for all

tornadoes within each cluster shows that the boundary zone cluster (cluster 3) was responsible for 25.9% of the DPI associated with the afternoon–evening supercells (Table 5). The high DPI and number of significant tornadoes, despite the lower median pathlengths, path width, and smaller fraction of significant tornadoes, is attributed to the combination of cluster 3 still containing numerous large, violent tornadoes

---

[7] DPI is defined as the product of path length, path width, and the EF-rating plus one.
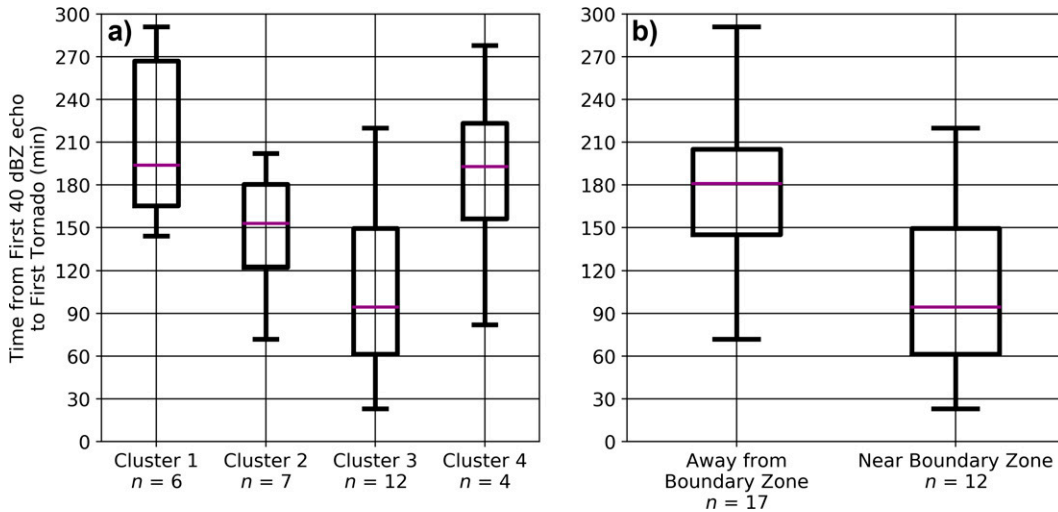
FIG. 14. Box-and-whisker plots of Δt_{CI-TG} (a) broken down by initiation cluster and (b) combining clusters 1, 2, and 4 ("Away from Boundary Zone") to cluster 3 ("Near Boundary Zone"). The number of supercells is given by n.

(particularly tornado M1, the Hackleburg–Phil Campbell–Tanner–Harvest, Alabama, EF5, which accounted for a DPI of 765.00%, 57.6% of the cluster's total DPI) and the larger number of total tornadoes (and parent supercells) in the cluster.

The effects of the boundary zone cannot be assumed to have been limited to the cells that initiated near it. The importance of the remnant outflow boundary zone is even more apparent when considering the individual tornadoes as opposed to the parent supercell and tornado family characteristics. When the proximity of each tornado (as defined by the start location and time) is compared to the approximate location of the thermal boundary zone in the RUC analyses, 65 of

the 102 tornadoes (63.7%) in the supercell episode formed near or north of (within about 50 km) the boundary zone, with the remaining 37 (36.3%) forming to its south (Fig. 18). Despite the much higher fraction of tornadoes that formed near the thermal boundary zone, the number of significant (EF2+) tornadoes was nearly the same (22 along/north of the boundary zone, 21 to its south), and the total pathlength and DPI were higher for the tornadoes south of the boundary zone than those along/north of it (Table 6). These findings counter those of Markowski et al. (1998) and Rasmussen et al. (2000), which found that 70% of tornadoes in the Verification of the Origins of Rotation in Tornado Experiment (VORTEX) were associated with boundaries external to the storm and
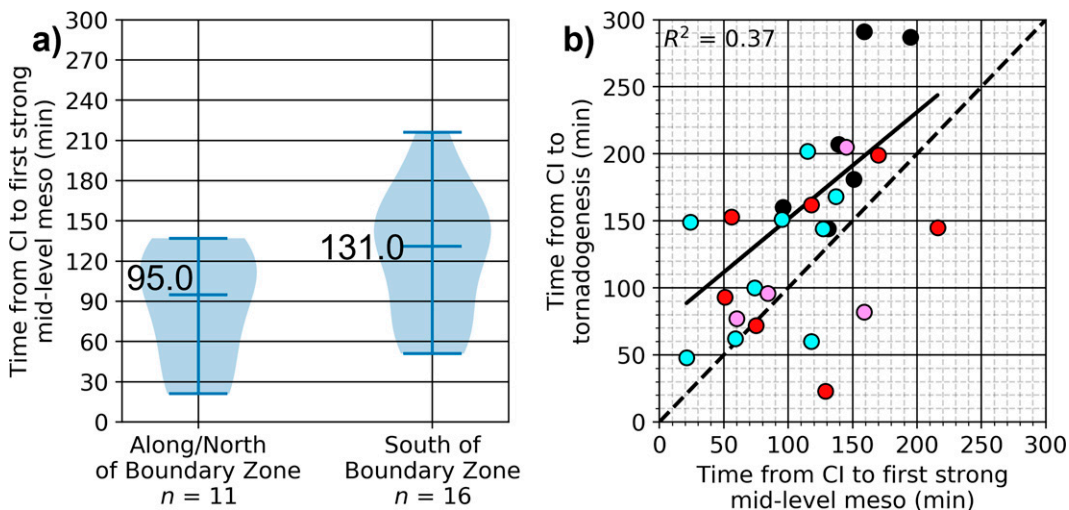
FIG. 15. (a) Violin plots of time from CI to strong midlevel mesocyclogenesis for storms that form along/north of the boundary zone (left violin plot) vs those that form south of the boundary zone (right violin plot), with the median time elapsed provided by the numbers. (b) Scatterplot of Δt_{CI-TG} as a function of time from CI to strong midlevel mesocyclogenesis, distinguished by initiating cluster.
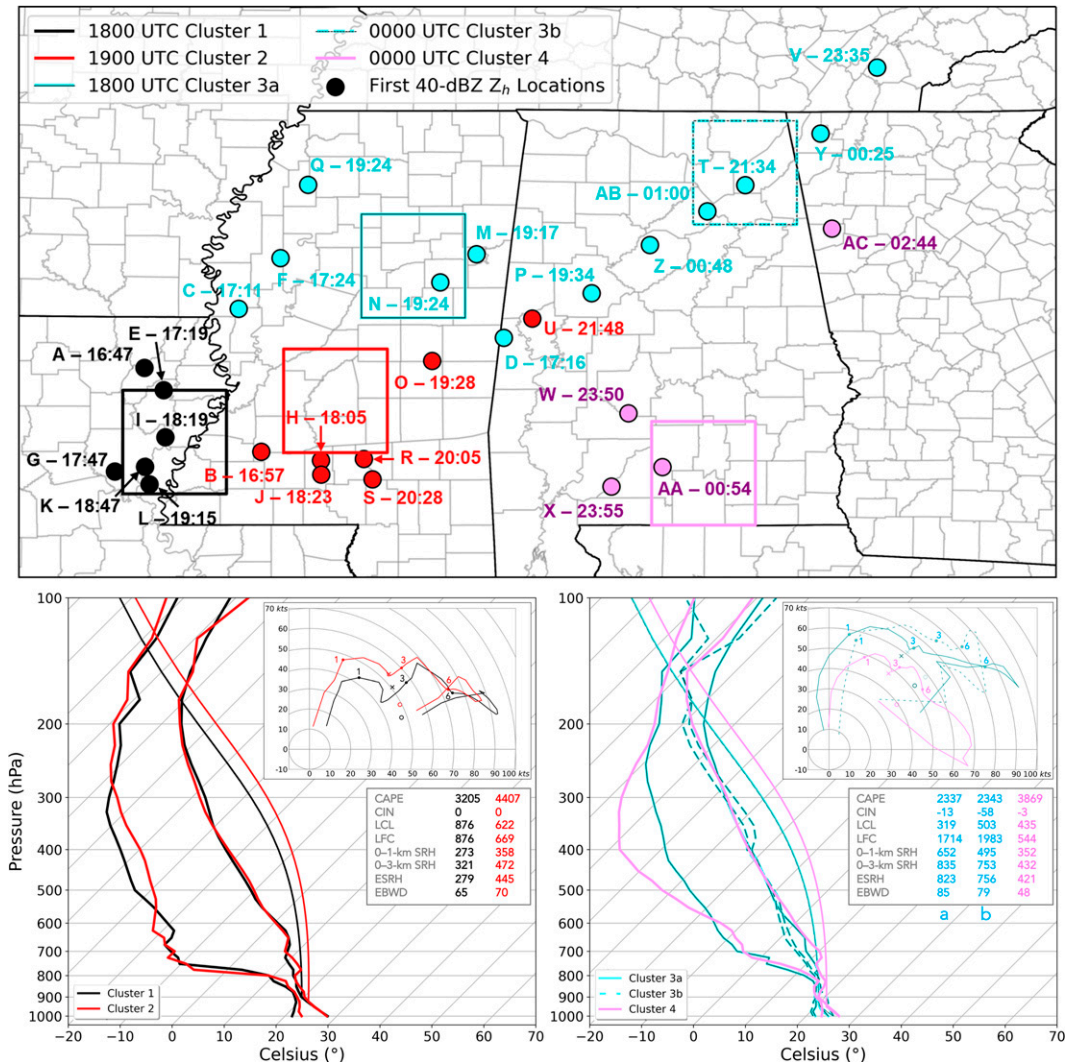
FIG. 16. RUC analysis area-mean soundings and hodographs representing the environments of each of the four initiating clusters of supercells described in Fig. 13. Soundings for (bottom left) clusters 1 and 2 and (bottom right) clusters 3 and 4 are provided. (top) Each sounding represents a 1° latitude × 1° longitude area depicted by the boxes on the map. The analysis time of each sounding is provided in the map legend, along with the cluster that each sounding represents. The points represent the CI location for each supercell, matched by cluster (color) and annotated by supercell ID letter and CI time (UTC). Convective available potential energy (CAPE; J kg^{-1}), convective inhibition (CIN; J kg^{-1}), lifting condensation level (LCL; m), and level of free convection (LFC; m) are provided for surface-based parcels. Values for 0–1-km SRH, 0–3-km SRH, effective inflow SRH (ESRH) are in m^2 s^{-2}, and effective inflow bulk wind difference is in knots (1 kt ≈ 0.51 m s^{-1}). The × symbol for each hodograph marks the estimated mean initial cell motion developed in Flournoy et al. (2021), and the o symbol marks the Bunkers right-moving motion estimates (Bunkers et al. 2000). The 1-, 3-, and 6-km AGL elevations are marked on each hodograph. Two soundings (3a and 3b) are provided to represent cluster 3 given its inter-storm spatiotemporal variability, and the parcel paths for those two soundings closely overlap.

speculated that boundaries may be necessary for the development of significant tornadoes, even in seemingly favorable background environments.

At initial glance, the statistics of the tornadoes that formed along/north of the boundary zone versus those that formed south of the boundary zone—as well as the statistics for tornadoes associated with supercells that formed near the boundary zone (cluster 3) against those that formed elsewhere—appear to paint a contradictory picture. Nearly an equal number of significant (EF2+) tornadoes occurred near the boundary zone as did in the open warm sector, and some of the most violent damage observed occurred with tornadoes in the boundary zone. The majority of violent tornadoes (9 of 15) occurred along/north of the
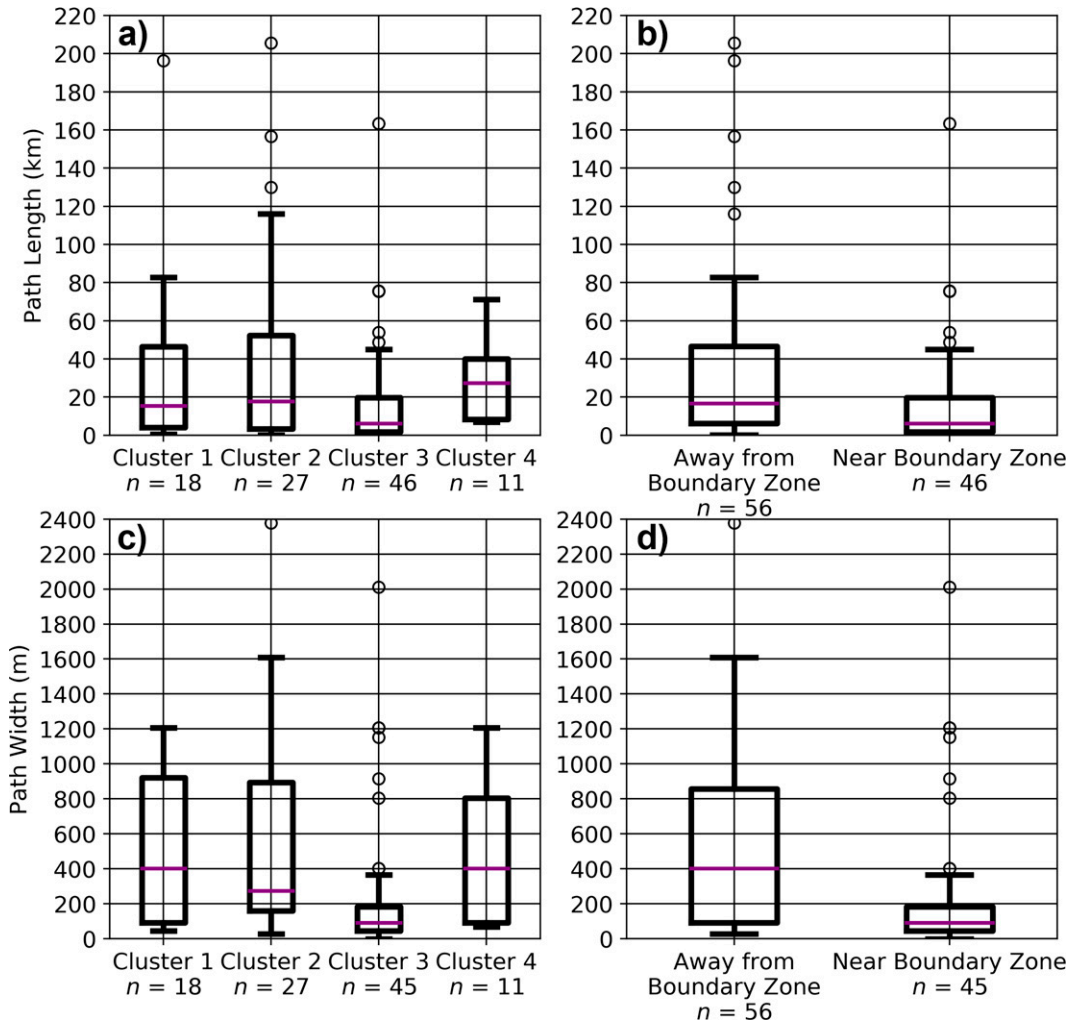
FIG. 17. As in Fig. 14, but for (a),(b) pathlength and (c),(d) path width. The number of tornadoes produced by supercells that initiated in each cluster is denoted by n. Note that $n = 45$ for cluster 3 and for "Near Boundary Zone" for path width, owing to the unknown path width of tornado M2.

thermal boundary, three of which were rated EF5 (out of four total in the outbreak). But despite this, and despite a strong majority of the tornadoes in the supercell phase of the outbreak occurring in the boundary zone, the total pathlength and DPI for the tornadoes south of the

boundary zone exceeds the values observed along the boundary zone.

A closer inspection of the significant tornadoes between the two groups indicates that the key difference is in the upper tails of their pathlength distributions (Fig. 19). Of the

TABLE 5. Breakdown of tornado counts by EF rating, total tornado count in each cluster ("Total Tor Count"), fraction of all tornadoes that were significant (EF2+; "Sig Tornado Fraction"), total DPI, total pathlength (PL), mean DPI of each tornado, and mean PL of each tornado within each cluster. DPI is computed in mi.^{2} to retain consistency with Thompson and Vescio (1998). The total of all pathlengths is 0.01 km off the sum of the individual cluster pathlengths due to rounding.

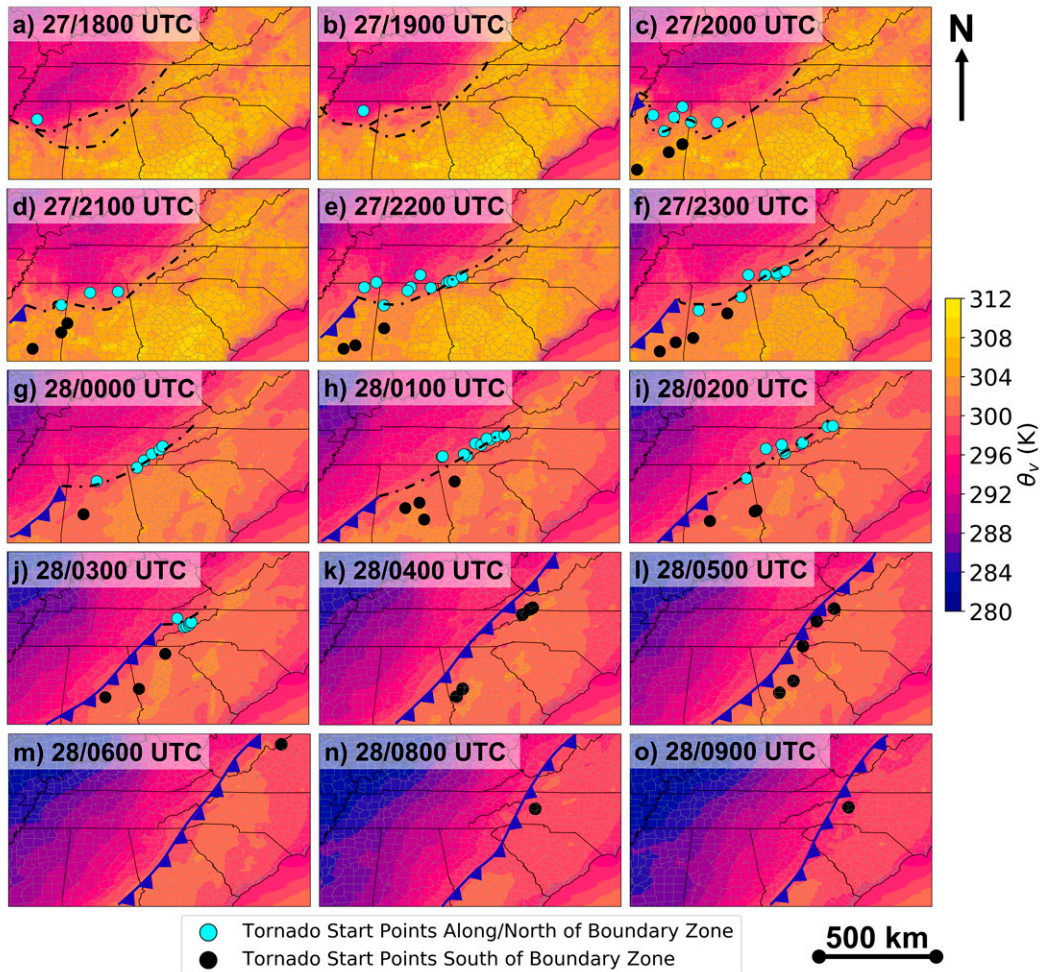|	EF0/unk	EF1	EF2	EF3	EF4	EF5	Total tor count	Sig tornado fraction (%)	Total DPI (mi.^{2})	Total PL (km)	Mean DPI (mi.^{2})	Mean PL (km)
Cluster 1	5	2	2	6	2	1	18	61.1	986.40	588.92	54.80	32.72
Cluster 2	6	8	2	5	4	2	27	48.1	2506.80	1079.93	92.84	40.00
Cluster 3	21	11	6	3	4	1	44	31.8	1328.83	758.74	28.89	16.49
Cluster 4	0	6	2	2	1	0	11	45.5	317.43	304.42	28.86	27.67
Total	32	27	12	16	11	4	102	42.2	5139.46	2732.02	50.89	26.79

FIG. 18. RUC surface θ_v analyses valid at (a) 1800 UTC 27 Apr, (b) 1900 UTC 27 Apr, (c) 2000 UTC 27 Apr, (d) 2100 UTC 27 Apr, (e) 2200 UTC 27 Apr, (f) 2300 UTC 27 Apr, (g) 0000 UTC 28 Apr, (h) 0100 UTC 28 Apr, (i) 0200 UTC 28 Apr, (j) 0300 UTC 28 Apr, (k) 0400 UTC 28 Apr, (l) 0500 UTC 28 Apr, (m) 0600 UTC 28 Apr, (n) 0800 UTC 28 Apr, and (o) 0900 UTC 28 Apr. Large dots indicate the locations of tornado start points within ±30-min windows surrounding each analysis time, with blue dots signifying tornadoes that formed along and north of the remnant thermal boundary zone and black dots representing tornadoes that formed south of the thermal boundary zone. Boundaries are analyzed as in Fig. 13. The 0700 UTC analysis is omitted because no tornadoes formed within the ±30-min window.

eight tornadoes during the entire 26–28 April 2011 outbreak that had pathlengths exceeding 80 km (50 mi.), seven occurred during the afternoon/evening supercell episode in the Southeast. Of those seven, only two (A1 and M1) occurred along the thermal boundary zone. The remaining five (J1, L1, O1, R1, and U1) occurred south of the boundary zone. Tornado M1 had a pathlength of 164.15 km and A1 had a pathlength of 82.80 km, while the five longest paths south of the boundary zone ranged from 116.08 to 205.67 km. These five tornadoes accounted for 804.63 of the 1543.84 km (52.1%) of total

TABLE 6. As in Table 5, but stratified by tornadoes that formed along/north of the thermal boundary zone vs tornadoes that formed south of the thermal boundary zone.

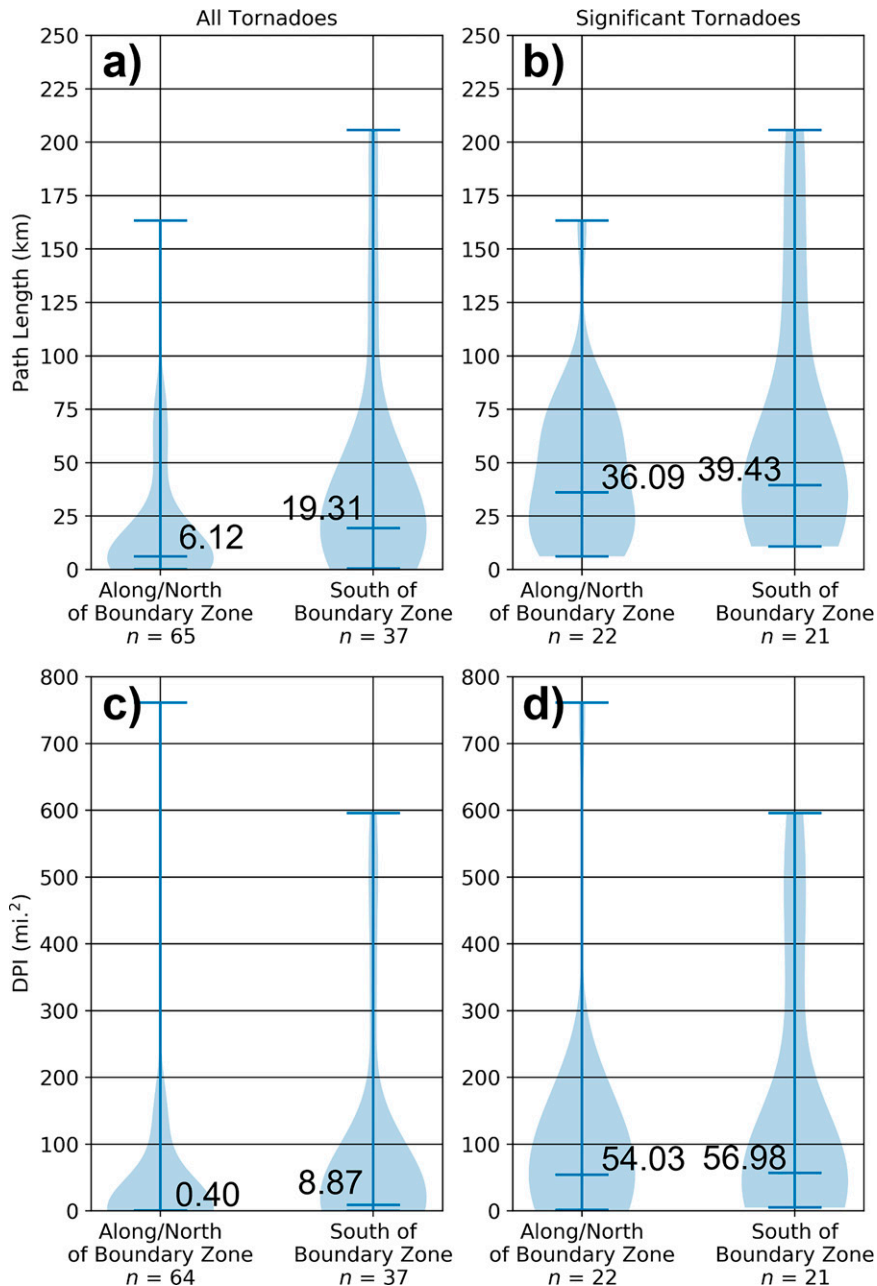|	EF0/unk	EF1	EF2	EF3	EF4	EF5	Total tor count	Sig tornado fraction (%)	Total DPI (mi.^{2})	Total PL (km)	Mean DPI (mi.^{2})	Mean PL (km)
Along/N of boundary zone	29	14	7	6	6	3	65	33.8	2154.06	1188.18	33.66	18.28
S of boundary zone	3	13	5	10	5	1	37	56.8	2985.40	1543.84	80.69	41.73
Total	32	27	12	16	11	4	102	42.2	5139.46	2732.02	50.89	26.79

FIG. 19. Violin plots of (a),(b) pathlength and (c),(d) DPI for (a),(c) all tornadoes and (b),(d) significant tornadoes, split by those along/north of the thermal boundary zone and those that began south of the boundary zone. Numbers on each plot depict median values. Note that DPI along/north of the boundary zone has one fewer observation because DPI was not calculated for tornado M2, given its unknown damage intensity and path width.

pathlength south of the boundary zone, skewing the mean values of both pathlength and DPI and heavily influencing the sums of pathlength and DPI. When the median values for pathlength and DPI of significant tornadoes along/north and south of the boundary zone are compared, the difference is small (Fig. 19).

In addition to being associated with a prolific number of tornadoes, the boundary zone also appeared to enhance the potential for tornadogenesis in supercells that had otherwise previously been unable to produce tornadoes. Supercells A, E, and I, all of which initiated in cluster 1 in the Louisiana Delta region, were dormant (with respect to tornado production) from the time of CI until they reached the boundary zone, when each produced EF3 tornadoes (Fig. 20). The dormant periods during the early life cycles of supercells E and I
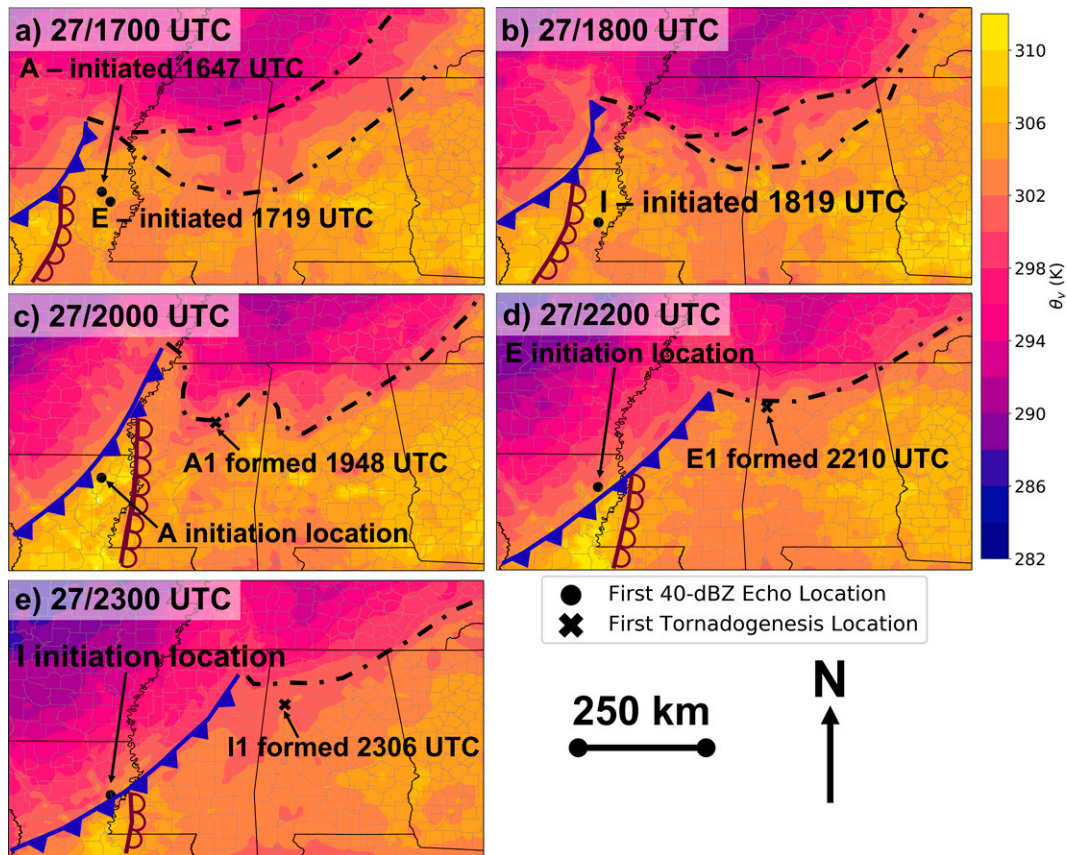
FIG. 20. RUC surface θ_v analyses closest to the times of CI of (a) supercells A and E at 1700 UTC 27 Apr and (b) supercell I at 1800 UTC 27 Apr; and closest to the times of first tornadogenesis for (c) supercell A at 2000 UTC 27 Apr, (d) supercell E at 2200 UTC 27 Apr, and (e) supercell I at 2300 UTC 27 Apr. Boundaries are analyzed as in Fig. 13.

were especially noteworthy given that they were the two longest periods from CI to tornadogenesis of all the supercells, at 4 h 51 min and 4 h 47 min, respectively.

We investigated regional differences in the relationship between $\Delta t_{\text{CI-TG}}$ and early-storm rotational characteristics in Fig. 21, with the primary hypothesis being that some of the spread in early evolutionary traits is linked to differences in the background environment (stratified by geographic region; Fig. 16). Figure 21 illustrates the relationship between both initial 0–3- and 3–6-km AzShear and $\Delta t_{\text{CI-TG}}$, distinguished by CI cluster. Many relationships between these characteristics (or the lack thereof) are evident in this figure. These include the following:

- There is a slight trend for supercells with greater initial azimuthal shear to take less time to produce a tornado; however, this trend is not significant and is likely influenced by the relative sparsity of points with initial azimuthal shear > 0.006 s^{-1}.
- *Regional differences across this parameter space exist, suggesting that different supercell evolutionary paths occurred in each region.* The clearest signal is that cluster 3 storms tend to reside in the upper-left part of the distribution, suggesting they typically contained stronger initial midlevel

mesocyclones (mean 3–6-km AzShear near 0.0055 s^{-1}) and took less time to produce their first tornadoes than storms in other regions (mean near 110 min). Conversely, cluster 1 storms contained weaker initial midlevel mesocyclones (mean 3–6-km AzShear near 0.0036 s^{-1}) and took longer to produce their first tornadoes (mean near 210 min).

c. Intra-cluster storm evolution variability

While broad trends in supercell and tornado characteristics applied to each of the clusters and with respect to the proximity of the thermal boundary zone, there was still large variability in supercell and tornado behavior within clusters, even near the boundary zone. Perhaps the most poignant example of within-cluster variability is between supercells M and N, located in cluster 3 (Fig. 22). The two supercells initiated approximately 44 km and 7 min apart from each other in northeastern Mississippi, both close to the thermal boundary zone depicted in Fig. 13c, but then evolved in radically different ways. Supercell M matured extraordinarily quickly, with genesis of tornado M1 (the Hackleburg–Phil Campbell–Tanner–Harvest EF5) occurring only 48 min after CI, while supercell N took 2 h 29 min to produce tornado N1 after CI. Supercell N also never produced a tornado that caused damage worse than EF1,
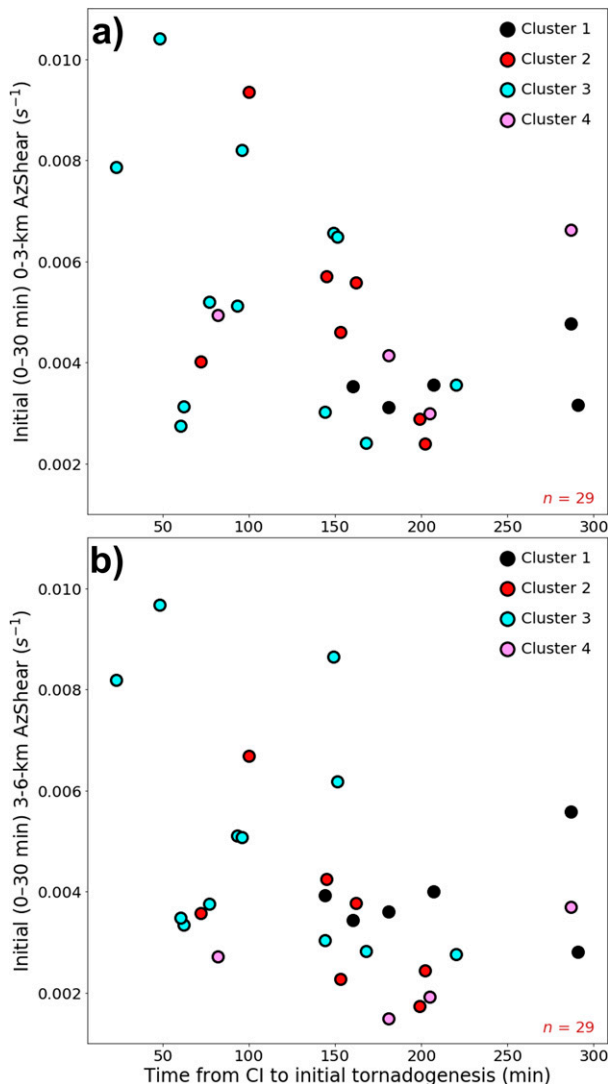
FIG. 21. Scatterplots of (a) initial (0–30 min after CI) 0–3-km AzShear and (b) midlevel (3–6 km AGL) AzShear as a function of $\Delta t_{\text{CI–TG}}$ for the clusters in which each tornadic storm (n = 29) initiated.

despite retaining supercellular characteristics for a much longer time and distance than supercell M. The remarkable disparities in the evolutions of supercells M and N serve as critical reminders of the potential roles that smaller-scale near-storm boundary layer heterogeneities, cell mergers/interactions, and internal stochastic processes may play in determining the outcomes of two cells forming in what may appear to be the same environment, even if that environment seems to be extremely supportive of violent tornadoes (Fig. 16).

Another noteworthy aspect of the 27–28 April supercells is that several experienced prolonged dormant periods between tornadoes. Of the 29 supercells, five of them experienced a dormant period of 2 h or greater: supercells E, I, N, R, and T (Fig. 23). While the dormant period with supercell T occurred northeast of the heart of the primary outbreak region, the

dormant periods of supercells E, I, N, and R occurred in the heart of the outbreak area, standing in stark contrast to other prolific, cyclic tornadic supercells that also occurred nearby in time and space. For example, supercell O, the most prolific supercell of the outbreak, followed a path similar to supercells E, I, and N. Supercell O preceded E by about 50 min and N by about an hour, and I followed behind O by about an hour (Fig. 24). The presence of the thermal boundary zone across north Alabama and east Tennessee may have played a role in the evolutions of these storms, with the dormant periods of E, I, and N occurring mostly in the cooler air northwest of the surface θ_v gradient, while supercell O followed a path on the warm edge of the θ_v gradient. However, supercell E did eventually produce tornadoes, including the violent (EF4) tornado E2, while still on the cool side of the boundary zone (Fig. 24d). Meanwhile, supercell R followed a very close path to supercell U and was less than an hour behind it (Fig. 24). Despite the close spatiotemporal proximity of R and U, the two supercells behaved remarkably differently across east-central Alabama and northern Georgia. Supercell U produced two EF3 tornadoes and one EF4 tornado completely within the spatial range of the dormant gap of supercell R. It is plausible that storm-scale impacts on the environment may also impact tornado potential on proximate storms, such as effects from supercell U on supercell R, but these impacts cannot be resolved in the RUC analyses.

Furthermore, supercell R featured remarkably strong AzShear values during a substantial portion of its dormant phase. Between 0100 and 0300 UTC, the AzShear values associated with supercell R rivaled the values associated with the intensely tornadic supercell U (Fig. 25) and far exceeded the mean AzShear values associated with the nontornadic phases of the supercells described in section 4, with 0–3-km AzShear briefly exceeding 0.03 s^{-1}, a value commonly associated with an ongoing violent tornado as indicated in Fig. 25a. The differences in behavior between supercells E, I, and N versus O and between supercells R and U further underscore the importance of small-scale environmental variability, convective interactions, and internal stochastic processes in supercell evolution and tornado production, even in a climatologically exceptional background environment. The high AzShear values during supercell R's dormant period also highlight the need to use some caution when diagnosing tornado potential with a given storm, despite the favorable differences in AzShear between tornadic and nontornadic phases of storms described in section 4.

6. Summary and conclusions

This study presents the first thorough classification to date of the historic round of destructive supercells and tornadoes that impacted the Southeast United States on 27–28 April 2011, as well as a detailed analysis of their traits. In all, 29 supercells were responsible for 102 tornadoes, 43 of which were significant (EF2+), and 313 fatalities across Alabama, Mississippi, Tennessee, Georgia, North Carolina, and Virginia. In total, 23 of the 29 supercells produced significant tornadoes, and 23 of the 102 tornadoes produced fatalities.
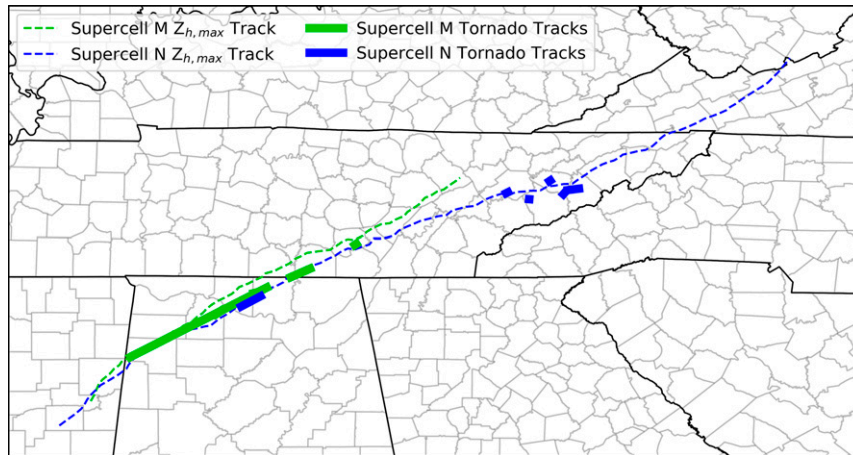
FIG. 22. Map of the supercell tracks, denoted by maximum Z_h as in Fig. 2, and tornado tracks associated with supercells M and N. Tornado identifiers and EF ratings are provided for reference.

Analysis of supercell characteristics and of the MYRORSS AzShear observations associated with the supercells reveals the following important findings:

1) There were four primary initiation clusters into which each of the 29 tornadic supercells fell:
    (i) Six supercells that initiated near the Mississippi River in the Louisiana Delta;
    (ii) Seven supercells that initiated in the open warm sector in a corridor from southern Mississippi to west-central Alabama;
    (iii) Twelve supercells that initiated in the vicinity of a remnant thermal boundary zone left by the first two QLCSs of the outbreak across northern Mississippi, northern Alabama, far northwestern Georgia, and east Tennessee; and
    (iv) Four supercells that initiated in a corridor from southern Alabama to western Georgia.
2) Supercells that formed in the cluster near the thermal boundary zone produced strong midlevel mesocyclones and tornadoes faster than those that formed farther south in the warm sector or nearer the dryline in the Louisiana Delta that was analyzed in CK22a.
3) The initiation cluster near the boundary zone featured the greatest number of supercells and tornadoes of any of the four clusters. These supercells featured a wide
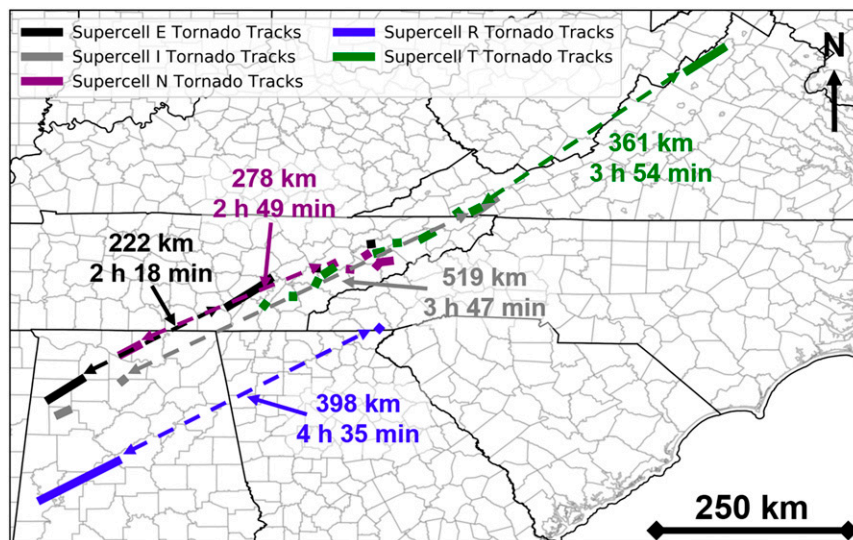
FIG. 23. Map highlighting the extended dormant periods between tornadoes associated with supercells E, I, N, R, and T. The distance between tornadoes at each end of the dormant periods and the durations of each dormant period are annotated.
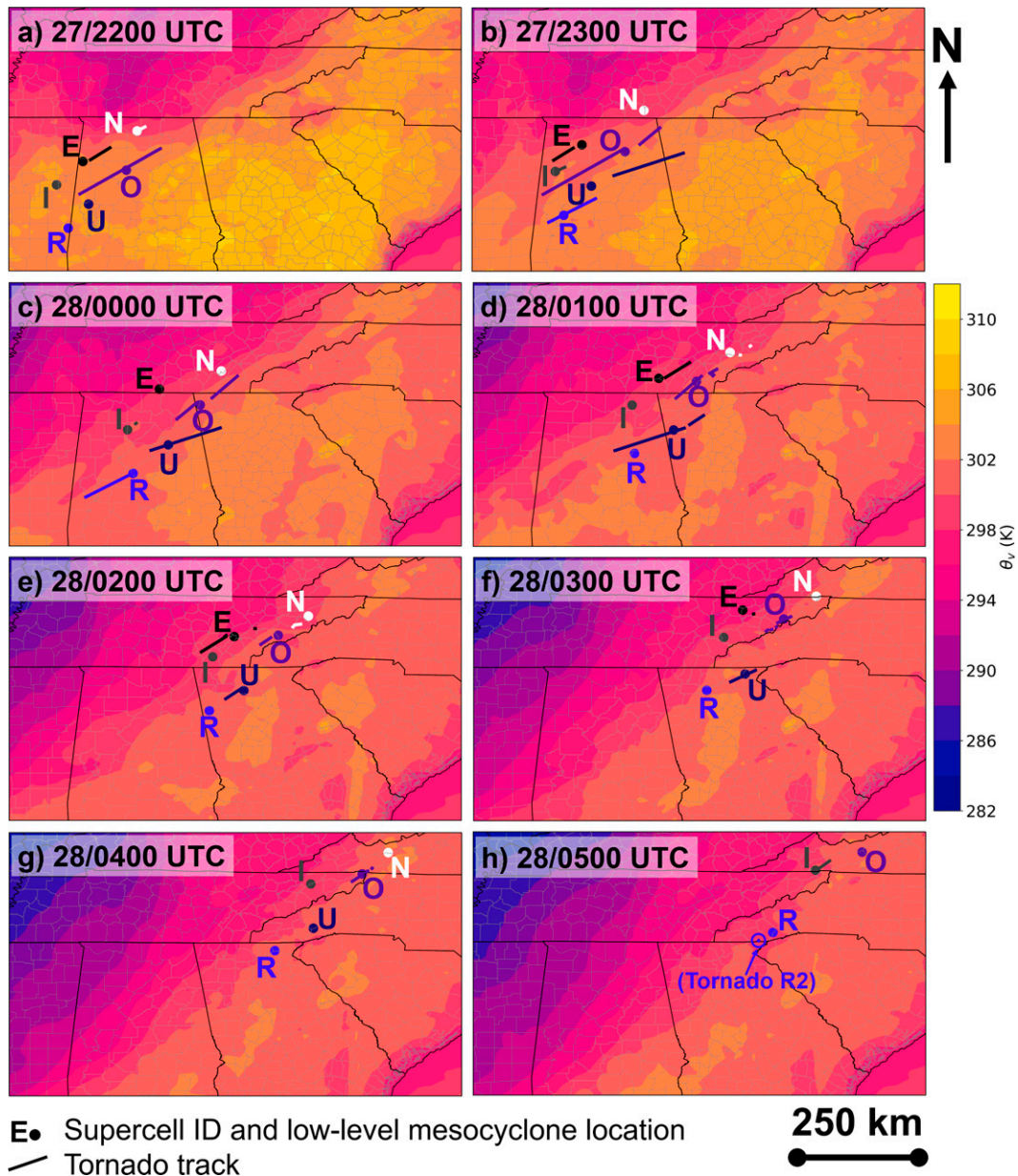
FIG. 24. RUC surface θ_v analyses at (a) 2200 UTC 27 Apr, (b) 2300 UTC 27 Apr, (c) 0000 UTC 28 Apr, (d) 0100 UTC 28 Apr, (e) 0200 UTC 28 Apr, (f) 0300 28 Apr, (g) 0400 UTC 28 Apr, and (h) 0500 UTC 28 Apr. The positions of the low-level mesocyclones of supercells E, I, N, O, R, and U, as approximated by the location of the maximum 0–3-km AzShear, are provided for each analysis time. Tornado tracks shown at each time are tornadoes that occurred, at least in part, within a $\pm$30 min window of the RUC analysis hour. Analyzed surface boundaries are omitted for clarity.

diversity of behavior, from long-lived violent tornadoes to cyclic genesis of numerous weak, short-lived tornadoes. Supercells in the initiating clusters farther to the south were more dominated by long-lived, significant tornado production.

4) A total of 65 of the 102 tornadoes were found to originate along/north of the thermal boundary zone remnant from the first two QLCSs during the outbreak, with the remaining 37 tornadoes forming south of the boundary zone. The total population of boundary-zone-associated tornadoes exhibited a wide array of behavior. While a nearly equal number of significant tornadoes occurred along/north of the boundary zone as did south of the boundary zone and a majority of the violent tornadoes observed occurred along/north of the boundary zone, the total pathlength and DPI of the tornadoes south of the
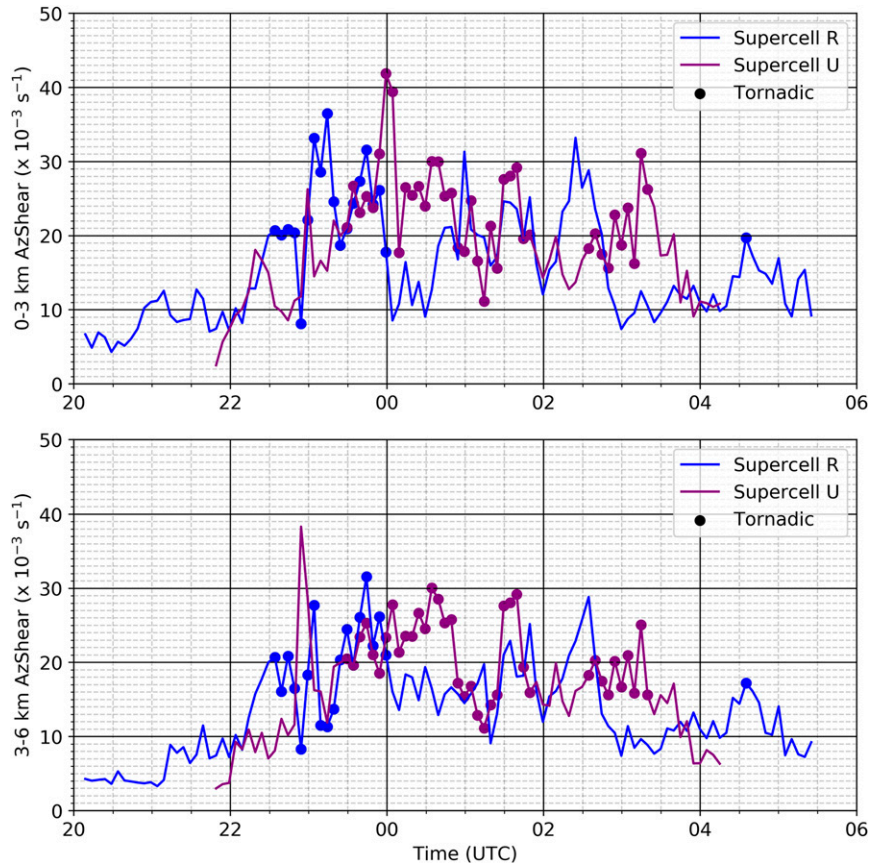
FIG. 25. Time series plots of (a) 0–3- and (b) 3–6-km AzShear for supercells R and U. Tornadic
AzShear observations are denoted by the markers.

boundary zone were greater. The longer total pathlength and higher DPI south of the boundary zone was driven by the occurrence of five very long-tracked tornadoes, with pathlengths ranging from 116.18 to 205.67 km. Only one tornado with a pathlength in that range was observed along or north of the boundary zone. *These observations lead to a proverbial double-edged sword with respect to the likely role of the boundary zone in the evolution of the outbreak.* On one hand, the boundary zone proved an extremely favorable environment for the formation of tornadoes of all intensities. And given that just short of half of the observed DPI from the event was accumulated in the boundary zone and the boundary zone itself represented a relatively concentrated corridor from north-central Mississippi across northern Alabama and east Tennessee, that region experienced an extraordinary level of risk to life and property. However, the majority of very long-tracked tornadoes being observed south of the thermal boundary zone may serve as circumstantial evidence that a relatively homogeneous environment is necessary to maintain tornadoes for excessively long time periods.

5) Storms that initiated in other areas and approached the thermal boundary zone exhibited notable changes in behavior. For example, supercells A, E, and I all initiated

in the Louisiana Delta and remained nontornadic for approximately 3–5 h until reaching the boundary zone, upon when each produced EF3 tornadoes. The long dormant periods each of these supercells exhibited prior to reaching the boundary zone suggest that the boundary zone may have been a key influence in these storms producing tornadoes.

6) Even within initiation clusters, a wide diversity of supercell behaviors was observed. For example, of two supercells that initiated only 44 km away and 7 min apart from each other, one produced an EF5 tornado 48 min after CI (supercell M) and the other only produced EF0–EF1 tornadoes during its entire life cycle (supercell N).

7) There were five instances of supercells experiencing dormant periods of 2 h or more between tornado production in relatively close spatiotemporal proximity to other supercells producing long-lived, intense tornadoes and/or undergoing frequent cyclic production. Three of those supercell dormant periods (supercells E, I, and N) may have been influenced by the thermal boundary zone, but that was not universally true for all five periods. For example, one supercell (U) that initiated in the southern Mississippi–west-central Alabama cluster produced three EF3–EF4 tornadoes in northern Alabama and northern

TABLE A1. Description and justification for changes made to the tornado tracks in this study from the official *Storm Data*/ONETOR dataset.

Supercell ID	Tornado No.	Description of change	Justification
D	2	Changed injury total from 50 to unknown.	*Storm Data* lists zero injuries across Jackson and DeKalb Counties in Alabama, where 12 of the 14 fatalities with this tornado occurred and near-EF5 damage occurred.
	8	Adjusted the start and end times backward 1 h from 2335 and 2337 UTC to 2235 and 2237 UTC, respectively.	Apparent time zone error, with no convection present in Bradley County, Tennessee, at 2335 UTC.
E	2	Adjusted the start and end times backward 1 h from 0206 and 0241 UTC to 0106 and 0141 UTC, respectively.	This is an apparent time zone error, with no mesocyclone evident near the tornado start point in Sequatchie County, Tennessee, at 0206 UTC, but an intense mesocyclone present around 0106 UTC.
	3	The start and end times applied in this paper are adjusted from 0228 and 0235 UTC to 0108 and 0115 UTC, respectively.	As with tornado E2, this tornado was adjusted backward 1 h for a time zone error. An additional backward adjustment of 20 min from the official start and end times was applied as no mesocyclone was evident on radar at the time of the official SPC track entry in the vicinity of the damage track. Radar analysis indicates this was most likely another tornado associated with supercell E, which is how it is assessed in this manuscript.
	4	The start and end times applied in this paper are adjusted from 0128 and 0133 UTC to 0138 and 0143 UTC, respectively.	No mesocyclone is present on radar in the vicinity of this tornado at the official *Storm Data* entry times. The mesocyclone associated with Storm E is present around 10 min later. Therefore, a 10-min adjustment forward in time is applied here.
M	1	This tornado track is terminated after 164.15 km (102 mi.) at 2150 UTC.	The official SPC entry for this tornado connects this track to tornado M4. Radar observations from the Hytop WSR-88D radar (KHTX) indicate a likely dissipation of this tornado in northern Madison County. Analysis of aerial nadir-pointing damage imagery and data from the University of Alabama in Huntsville's (UAH) Advanced Radar for Meteorological and Operational Research (ARMOR) conducted by Burke et al. (2019) found evidence of the tornado track ending in Madison County. Furthermore, the tornado track information in the NWS's Damage Assessment Toolkit also ends the track near the radar- and aerial-imagery-suggested damage location near the Hazel Green community (Fig. A1), and the official *Storm Data* entry for the Madison County, Alabama, segment of this tornado describes a substantial weakness or break in the damage track in northern Madison County. The track information in the DAT is the basis for the pathlength used herein.
		The death toll is revised downward from the 72 in *Storm Data* to 71.	The death toll was revised downward by 1 to account for the double-counting of the death of a Phil Campbell (Franklin County, Alabama) resident who died at the Wrangler jeans factory in Hackleburg (Marion County, Alabama). This double-count was confirmed in personal communication with NWS Huntsville personnel.
		The injury total was revised from 145 to unknown.	*Storm Data* lists a total of 145 injuries: 100 in Marion County and 45 in Limestone County. No injuries are attributed to Franklin, Lawrence, or Madison Counties, which combined for a total of 49 of the tornado's 71 fatalities. Given the likelihood of an extreme underestimation of the injury count, the injury count is listed as unknown for the purposes of this manuscript.
	2	This tornado is not included in *Storm Data* but is included in this manuscript.	This anticyclonic tornado was detected by the UAH ARMOR radar in far northeastern Lawrence County, Alabama, located directly behind tornado M1, and indicated by both a tight anticyclonic rotational couplet and a polarimetric tornado debris signature. Because this tornado occurred completely within the path of the large, violent tornado M1, the pathlength of this tornado is estimated by the

TABLE A1. (*Continued*)

Supercell ID	Tornado No.	Description of change	Justification
			ARMOR data (available by request here: https://www.nsstc.uah.edu/swirll/main/live-data/index.php), and its path width and intensity are unknown.
	3	The end time for this satellite tornado was adjusted from 2145 to 2142 UTC.	This end time adjustment was made to account for the short pathlength and the fast translational speed of supercell M.
	4	This tornado was split from the *Storm Data* entry for tornado M1 and assigned a start time of 2208 UTC, an end time of 2240 UTC, a pathlength of 21.52 km, a path width of 400 m, a rating of EF3, and 0 deaths or injuries.	This tornado track is officially combined with tornado M1 in the ONETOR database. Radar data from the KHTX WSR-88D supports this tornado likely forming very close to the Alabama–Tennessee state line, on the border between Madison County, Alabama, and Lincoln County, Tennessee. Therefore, the information for this tornado is derived from the *Storm Data* county segment entries for Lincoln and Franklin Counties in Tennessee.
O	2	The injury total for this tornado was changed from 0 to unknown.	This tornado is credited with 25 fatalities but no injuries in the ONETOR database. Given the extreme damage intensity and high fatality count associated with this tornado, the idea of there being 0 injuries is completely unrealistic. Therefore, the injury count is marked as "unknown" in this manuscript.
W	4	The start time for this tornado was adjusted backward 5 min from 0250 to 0245 UTC.	The circulation appeared to be substantially down-track from the tornado start point by 0250 UTC.

Georgia. Roughly 1 h later, a second, previously tornadic supercell (R) tracked through the same region and did not produce any tornadoes there. *The close spatiotemporal occurrence of cyclic, significant tornado production to dormancy further emphasizes the need to better understand smaller-scale near-storm environmental heterogeneity on multiple scales, storm–environment interactions, cell mergers/interactions, and internal stochastic processes of supercells, even within a favorable background environment for tornadoes.*

8) Analysis of the period-mean AzShear for the nontornadic, pre-tornadic, and tornadic periods of each supercell indicate significant differences in mean 0–3- and 3–6-km AzShear between the three phases. Likewise, within the tornadic periods of each storm, the tornado-mean and tornado-maximum AzShear values showed significant skill in diagnosing whether the ongoing tornado(es) would produce a maximum of weak, strong, or violent damage. This relationship was strongest for the tornado-maximum 0–3-km AzShear observations. These observations suggest that AzShear may be directly useful to the tornado warning process in discriminating between nontornadic, pre-tornadic (i.e., within 30 min of tornadogenesis), and tornadic periods, as well as in discriminating between weak, strong, and violent tornadoes.

9) The mean pre-tornadic AzShear values in either the 0–3- or 3–6-km depths showed no skill in predicting the eventual peak tornado damage intensity.

10) Similar to single-Doppler V_{ROT} analysis, the ability for AzShear to distinguish between the likely maximum damage intensity of an ongoing tornado showed sensitivity to the distance from the nearest radar integrated into the AzShear product. While the maximum AzShear observed during weak and strong tornadoes was weakly affected by distance from the radar, the maximum AzShear was particularly sensitive to the distance from the nearest radar during violent tornadoes.

This study complements the work of K14, CK22a, and CK22b in documenting the prolific round of destructive supercells that impacted the Southeast United States on 27–28 April 2011. Our findings are novel in documenting storm-scale characteristics during the life cycles of each supercell, including the times of CI, tornadogenesis, and tornado demise, and low- and midlevel AzShear evolution along each supercell track. We hope that this study is useful to the community in providing a detailed summary of these historic supercells and tornado families, showing the usefulness of the MYRORSS dataset in examining storm-scale evolution, and documenting the variety of supercell evolutionary paths that occurred during this event. This study also serves to highlight the diversity of supercell behavior and evolution and its dependence on multiple scales of environment heterogeneity, even within a historically violent outbreak set within a classically favorable, synoptically evident tornado outbreak pattern (as depicted in CK22a). To our knowledge, these observational analyses are the first to document quantitative differences in mesocyclone evolution and tornado potential associated with supercells forming in very similar background environments; this complements recent modeling studies examining the volatility of tornado production in idealized supercells (e.g., Coffer et al. 2017; Flournoy et al. 2020; Markowski 2020).

We believe that additional storm-scale analyses of this detail (e.g., with respect to tornado production associated
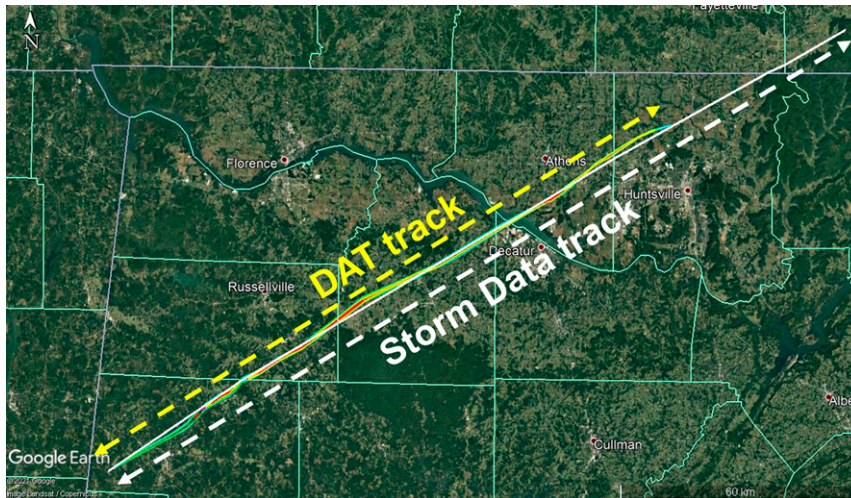
FIG. A1. Comparison map of tornado M1 from the DAT (polygons) and *Storm Data* (white line). Map generated in Google Earth.

with each supercell) would be helpful in further understanding general supercell evolutionary characteristics and processes. Several related questions arose during the course of this work, including: what storm-scale details/processes led to one supercell quickly producing a violent tornado while an adjacent storm took much longer to produce weak tornadoes? What local environmental heterogeneities were present on this day that supported certain clusters of storms to differ significantly in terms of evolutionary time scales and tornado production (even within the prolific, large-scale background environment)? How might such variations yield different supercell evolutions in other, less potent large-scale environments? Local topography may have been one particular source of environmental heterogeneity and potential local impacts on the supercells and tornadoes in this event, as was briefly addressed in K14. While this study does not seek to address any potential terrain influences, numerous past studies have focused on the role of terrain in severe storm environmental evolution and tornado behavior in areas impacted by this devastating round of supercells, including the Sand Mountain and Lookout Mountain plateaus in northeastern Alabama and far northwestern Georgia (Lyza and Knupp 2018; Lyza et al. 2020; Katona and Markowski 2021), the Appalachian Mountains (McKeown et al. 2021; Purpura et al. 2021), the Tennessee Valley in east Tennessee (Gaffin and Parker 2006; Schneider 2009), and the Cumberland Plateau in east Tennessee (Gaffin and Parker 2006; Gaffin 2012; Shamburger 2012). Further observational analyses like ours for multiple supercell events would be very helpful in addressing these questions, as well as ensembles of simulated supercells initialized in different environments. Finally, the ability of the MYRORSS AzShear dataset in identifying pre-tornadic periods should be examined in different environments to assess its potential usefulness for forecasters in real-time operational settings.

APPENDIX

Corrections to SPC Tornado Track Information

Table A1 describes changes made from the SPC database to the information supplied in this manuscript for each tornado associated with the 27–28 April 2011 supercells, along with justification for each change.

REFERENCES

Benjamin, S. G., G. A. Grell, J. M. Brown, T. G. Smirnova, and R. Bleck, 2004a: Mesoscale weather prediction with the RUC hybrid isentropic–terrain-following coordinate model. *Mon. Wea. Rev.*, **132**, 473–494, https://doi.org/10.1175/1520-0493(2004)132<0473:MWPWTR>2.0.CO;2.

——, and Coauthors, 2004b: An hourly assimilation–forecast cycle: The RUC. *Mon. Wea. Rev.*, **132**, 495–518, https://doi.org/10.1175/1520-0493(2004)132<0495:AHACTR>2.0.CO;2.

Boustead, J. M., B. E. Mayes, W. Gargan, J. L. Leighton, G. Phillips, and P. N. Schumacher, 2013: Discriminating environmental conditions for significant warm sector and boundary tornadoes in parts of the Great Plains. *Wea. Forecasting*, **28**, 1498–1523, https://doi.org/10.1175/WAF-D-12-00102.1.

Brotzge, J., and S. Erickson, 2010: Tornadoes without NWS warning. *Wea. Forecasting*, **25**, 159–172, https://doi.org/10.1175/2009WAF2222270.1.

Brown, R. A., B. A. Flickinger, E. Forren, D. M. Schultz, D. Sirmans, P. L. Spencer, V. T. Wood, and C. L. Ziegler, 2005: Improved detection of severe storms using experimental fine-resolution WSR-88D measurements. *Wea. Forecasting*, **20**, 3–14, https://doi.org/10.1175/WAF-832.1.

Bunkers, M. J., B. A. Klimowski, J. W. Zeitler, R. L. Thompson, and M. L. Weisman, 2000: Predicting supercell motion using a new hodograph technique. *Wea. Forecasting*, **15**, 61–79, https://doi.org/10.1175/1520-0434(2000)015<0061:PSMUAN>2.0.CO;2.

Burgess, D. W., L. R. Lemon, and V. T. Wood, 1975: Tornado characteristics revealed by Doppler radar. *Geophys. Res. Lett.*, **2**, 183–184, https://doi.org/10.1029/GL002i005p00183.

Burke, A. R., R. Wade, R. Griffin, A. W. Lyza, and D. M. Conrad, 2019: Analyzing tornadic debris signatures by integrating aerial imagery and polarimetric radar data in GIS. *Special Symp. on Meteorological Observations and Instrumentation*, Phoenix, AZ, Amer. Meteor. Soc., 1.6, https://ams.confex.com/ams/2019Annual/webprogram/Paper354293.html.

Chasteen, M. B., and S. E. Koch, 2022a: Multiscale aspects of the 26–27 April 2011 tornado outbreak. Part I: Outbreak chronology and environmental evolution. *Mon. Wea. Rev.*, **150**, 309–335, https://doi.org/10.1175/MWR-D-21-0013.1.

——, and ——, 2022b: Multiscale aspects of the 26–27 April 2011 tornado outbreak. Part II: Environmental modifications and upscale feedbacks arising from latent processes. *Mon. Wea. Rev.*, **150**, 337–368, https://doi.org/10.1175/MWR-D-21-0014.1.

Coffer, B. E., M. D. Parker, J. M. L. Dahl, L. J. Wicker, and A. J. Clark, 2017: Volatility of tornadogenesis: An ensemble of simulated nontornadic and tornadic supercells in VORTEX2 environments. *Mon. Wea. Rev.*, **145**, 4605–4625, https://doi.org/10.1175/MWR-D-17-0152.1.

Cohen, A. E., J. B. Cohen, R. L. Thompson, and B. T. Smith, 2018: Simulating tornado probability and tornado wind speed based on statistical models. *Wea. Forecasting*, **33**, 1099–1108, https://doi.org/10.1175/WAF-D-17-0170.1.

Davenport, C. E., 2021: Environmental evolution of long-lived supercell thunderstorms in the Great Plains. *Wea. Forecasting*, **36**, 2187–2209, https://doi.org/10.1175/WAF-D-21-0042.1.

Davies-Jones, R., 1984: Streamwise vorticity: The origin of updraft rotation in supercell storms. *J. Atmos. Sci.*, **41**, 2991–3006, https://doi.org/10.1175/1520-0469(1984)041<2991:SVTOOU>2.0.CO;2.

Doswell, C. A., III, 2007: Small sample size and data quality issues illustrated using tornado occurrence data. *Electron. J. Severe Storms Meteor.*, **2** (5), https://ejssm.org/archives/2007/vol-2-5-2007/.

Edwards, R., H. E. Brooks, and H. Cohn, 2021: Changes in tornado climatology accompanying the enhanced Fujita scale. *J. Appl. Meteor. Climatol.*, **60**, 1465–1482, https://doi.org/10.1175/JAMC-D-21-0058.1.

Flournoy, M. D., M. C. Coniglio, E. N. Rasmussen, J. C. Furtado, and B. E. Coffer, 2020: Modes of storm-scale variability and tornado potential in VORTEX2 near- and far-field tornadic environments. *Mon. Wea. Rev.*, **148**, 4185–4207, https://doi.org/10.1175/MWR-D-20-0147.1.

——, ——, and ——, 2021: Examining relationships between environmental conditions and supercell motion in time. *Wea. Forecasting*, **36**, 737–755, https://doi.org/10.1175/WAF-D-20-0192.1.

——, A. W. Lyza, M. A. Satrio, M. R. Diedrichsen, M. C. Coniglio, and S. Waugh, 2022: A climatology of cell mergers with supercells and their association with mesocyclone evolution. *Mon. Wea. Rev.*, **150**, 451–461, https://doi.org/10.1175/MWR-D-21-0204.1.

Fujita, T. T., D. L. Bradbury, and C. F. V. Thullenar, 1970: Palm Sunday tornadoes of April 11, 1965. *Mon. Wea. Rev.*, **98**, 29–69, https://doi.org/10.1175/1520-0493(1970)098<0029:PSTOA>2.3.CO;2.

Gaffin, D. M., 2012: The influence of terrain during the 27 April 2011 super tornado outbreak and 5 July 2012 derecho around the Great Smoky Mountains National Park. *26th Conf. on Severe Local Storms*, Nashville, TN, Amer. Meteor. Soc., 2, https://ams.confex.com/ams/26SLS/webprogram/Paper220492.html.

——, and S. S. Parker, 2006: A climatology of synoptic conditions associated with significant tornadoes across the southern Appalachian region. *Wea. Forecasting*, **21**, 735–751, https://doi.org/10.1175/WAF951.1.

Garner, J. M., 2012: Environments of significant tornadoes occurring within the warm sector versus those occurring along surface baroclinic boundaries. *Electron. J. Severe Storms Meteor.*, **7** (5), https://ejssm.org/archives/wp-content/uploads/2021/09/vol7-5.pdf.

Gibbs, J. G., 2016: A skill assessment of techniques for real-time diagnosis and short-term prediction of tornado intensity using the WSR-88D. *J. Oper. Meteor.*, **4**, 170–181, https://doi.org/10.15191/nwajom.2016.0413.

——, and B. R. Bowers, 2019: Techniques and thresholds of significance for using WSR-88D velocity data to anticipate significant tornadoes. *J. Oper. Meteor.*, **7**, 117–137, https://doi.org/10.15191/nwajom.2019.0709.

Johns, R. H., D. W. Burgess, C. A. Doswell III, M. S. Gilmore, J. A. Hart, and S. F. Piltz, 2013: The 1925 Tri-State tornado damage path and associated storm system. *Electron. J. Severe Storms Meteor.*, **8** (2), https://ejssm.org/archives/2013/vol-8-2-2013/.

Karstens, C. D., and Coauthors, 2016: Evaluation of near real-time preliminary tornado damage paths. *J. Oper. Meteor.*, **4**, 132–141, https://doi.org/10.15191/nwajom.2016.0410.

Katona, B., and P. Markowski, 2021: Assessing the influence of complex terrain on severe convective environments in northeastern Alabama. *Wea. Forecasting*, **36**, 1003–1029, https://doi.org/10.1175/WAF-D-20-0136.1.

Knupp, K. R., and Coauthors, 2014: Meteorological overview of the devastating 27 April 2011 tornado outbreak. *Bull. Amer. Meteor. Soc.*, **95**, 1041–1062, https://doi.org/10.1175/BAMS-D-11-00229.1.

Lyza, A. W., and K. R. Knupp, 2018: A background investigation of tornado activity across the southern Cumberland Plateau terrain system of northeastern Alabama. *Mon. Wea. Rev.*, **146**, 4261–4278, https://doi.org/10.1175/MWR-D-18-0300.1.

——, T. A. Murphy, B. T. Goudeau, P. T. Pangle, K. R. Knupp, and R. A. Wade, 2020: Observed near-storm environment variations across the southern Cumberland Plateau system in northeastern Alabama. *Mon. Wea. Rev.*, **148**, 1465–1482, https://doi.org/10.1175/MWR-D-19-0190.1.

Maddox, R. A., L. R. Hoxit, and C. F. Chappell, 1980: A study of tornadic thunderstorm interactions with thermal boundaries. *Mon. Wea. Rev.*, **108**, 322–336, https://doi.org/10.1175/1520-0493(1980)108<0322:ASOTTI>2.0.CO;2.

Magee, K. M., and C. E. Davenport, 2020: An observational analysis quantifying the distance of supercell-boundary interactions in the Great Plains. *J. Oper. Meteor.*, **8**, 15–38, https://doi.org/10.15191/nwajom.2020.0802.

Mahalik, M. C., B. R. Smith, K. L. Elmore, D. M. Kingfield, K. L. Ortega, and T. M. Smith, 2019: Estimates of gradients in radar moments using a linear least squares derivative technique. *Wea. Forecasting*, **34**, 415–434, https://doi.org/10.1175/WAF-D-18-0095.1.

Markowski, P. M., 2020: What is the intrinsic predictability of tornadic supercell thunderstorms? *Mon. Wea. Rev.*, **148**, 3157–3180, https://doi.org/10.1175/MWR-D-20-0076.1.

——, E. N. Rasmussen, and J. M. Straka, 1998: The occurrence of tornadoes in supercells interacting with boundaries during VORTEX-95. *Wea. Forecasting*, **13**, 852–859, https://doi.org/10.1175/1520-0434(1998)013<0852:TOOTIS>2.0.CO;2.

McKeown, K. E., C. Davenport, S. M. Purpura, and M. D. Eastin, 2021: Radar characteristics of observed supercell thunderstorms interacting with the Appalachian Mountains. *20th Annual Student Conf.*, online, Amer. Meteor. Soc., 109, https://ams.confex.com/ams/101ANNUAL/meetingapp.cgi/Paper/385001.

Miller, M. L., V. Lakshmanan, and T. M. Smith, 2013: An automated method for depicting mesocyclone paths and intensities. *Wea. Forecasting*, **28**, 570–585, https://doi.org/10.1175/WAF-D-12-00065.1.

NWS Jackson MS, 2021: NWS Jackson, MS April 26–27, 2011 severe weather outbreak. NWS, accessed 7 October 2021, https://www.weather.gov/jan/2011_04_25_27_svr.

Purpura, S. M., C. Davenport, K. E. McKeown, and M. D. Eastin, 2021: Environmental evolution of supercells interacting with the Appalachian Mountains. *20th Annual Student Conf.*, online, Amer. Meteor. Soc., 110, https://ams.confex.com/ams/101ANNUAL/meetingapp.cgi/Paper/385061.

Rasmussen, E. N., S. Richardson, J. M. Straka, P. M. Markowski, and D. O. Blanchard, 2000: The association of significant tornadoes with a baroclinic boundary on 2 June 1995. *Mon. Wea. Rev.*, **128**, 174–191, https://doi.org/10.1175/1520-0493(2000)128<0174:TAOSTW>2.0.CO;2.

Ryzhkov, A. V., T. J. Schuur, D. W. Burgess, and D. S. Zrnic, 2005: Polarimetric tornado detection. *J. Appl. Meteor.*, **44**, 557–570, https://doi.org/10.1175/JAM2235.1.

Schaefer, J. T., and R. Edwards, 1999: The SPC tornado/severe thunderstorm database. Preprints, *11th Conf. on Applied Climatology*, Dallas, TX, Amer. Meteor. Soc., 215–220.

Schneider, D. G., 2009: The impact of terrain on three cases of tornadogenesis in the Great Tennessee Valley. *Electron. J. Oper. Meteor.*, **10** (11), http://nwafiles.nwas.org/ej/pdf/2009-EJ11.pdf.

Shamburger, S. W., 2012: Higher terrain impacts of eastern middle Tennessee on tornadogenesis. *26th Conf. on Severe Local Storms*, Nashville, TN, Amer. Meteor. Soc., 9, https://ams.confex.com/ams/26SLS/webprogram/Paper211577.html.

Smith, B. T., R. L. Thompson, A. R. Dean, and P. T. Marsh, 2015: Diagnosing the conditional probability of tornado damage rating using environmental and radar attributes. *Wea. Forecasting*, **30**, 914–932, https://doi.org/10.1175/WAF-D-14-00122.1.

——, ——, D. A. Speheger, A. R. Dean, C. D. Karstens, and A. K. Anderson-Frey, 2020a: WSR-88D tornado intensity estimates. Part I: Real-time probabilities of peak tornado wind speeds. *Wea. Forecasting*, **35**, 2479–2492, https://doi.org/10.1175/WAF-D-20-0010.1.

——, ——, ——, ——, ——, and ——, 2020b: WSR-88D tornado intensity estimates. Part II: Real-time applications to tornado warning time scales. *Wea. Forecasting*, **35**, 2493–2506, https://doi.org/10.1175/WAF-D-20-0011.1.

Smith, T. M., and K. L. Elmore, 2004: The use of radial velocity derivatives to diagnose rotation and divergence. Preprints, *11th Conf. on Aviation, Range, and Aerospace*, Hyannis, MA, Amer. Meteor. Soc., P5.6, https://ams.confex.com/ams/pdfpapers/81827.pdf.

——, and Coauthors, 2016: Multi-Radar Multi-Sensor (MRMS) severe weather and aviation products: Initial operating capabilities. *Bull. Amer. Meteor. Soc.*, **97**, 1617–1630, https://doi.org/10.1175/BAMS-D-14-00173.1.

Thompson, R. L., and M. D. Vescio, 1998: The destruction potential index: A method for comparing tornado days. Preprints, *19th Conf. on Severe Local Storms*, Minneapolis, MN, Amer. Meteor. Soc., 280–282.

——, and R. Edwards, 2000: An overview of environmental conditions and forecast implications of the 3 May 1999 tornado outbreak. *Wea. Forecasting*, **15**, 682–699, https://doi.org/10.1175/1520-0434(2000)015<0682:AOOECA>2.0.CO;2.

——, and Coauthors, 2017: Tornado damage rating probabilities derived from WSR-88D data. *Wea. Forecasting*, **32**, 1509–1528, https://doi.org/10.1175/WAF-D-17-0004.1.

Weckwerth, T. M., J. Hanesiak, J. W. Wilson, S. B. Trier, S. K. Degelia, W. A. Gallus Jr., R. D. Roberts, and X. Wang, 2019: Nocturnal convection initiation during PECAN 2015. *Bull. Amer. Meteor. Soc.*, **100**, 2223–2239, https://doi.org/10.1175/BAMS-D-18-0299.1.

Welch, B. L., 1947: The generalization of 'Student's' problem when several different population variances are involved. *Biometrika*, **34**, 28–35, https://doi.org/10.2307/2332510.

Williams, S. S., K. L. Ortega, and T. M. Smith, 2020: Multi-year reanalysis of remotely sensed storms data. OSF, accessed 30 March 2021, https://doi.org/10.15763/DBS.CIMMS.MYRORSS.DATA.

——, ——, ——, and A. E. Reinhart, 2022: Comprehensive radar data for the contiguous United States: Multi-year reanalysis of remotely sensed storms. *Bull. Amer. Meteor. Soc.*, **103**, E838–E854, https://doi.org/10.1175/BAMS-D-20-0316.1.

Wilson, J. W., and R. D. Roberts, 2006: Summary of convective storm initiation and evolution during IHOP: Observational and modeling perspective. *Mon. Wea. Rev.*, **134**, 23–47, https://doi.org/10.1175/MWR3069.1.

WSEC, 2006: A recommendation for an enhanced Fujita scale (EF-scale). Wind Science and Engineering Center Rep., 108 pp., http://www.depts.ttu.edu/nwi/Pubs/FScale/EFScale.pdf.